THE JOURNAL OF PHYSICAL CHEMISTRY C

A JOURNAL OF THE AMERICAN CHEMICAL SOCIETY

June 24, 2021
Volume 125
Number 24
pubs.acs.org/JPCC

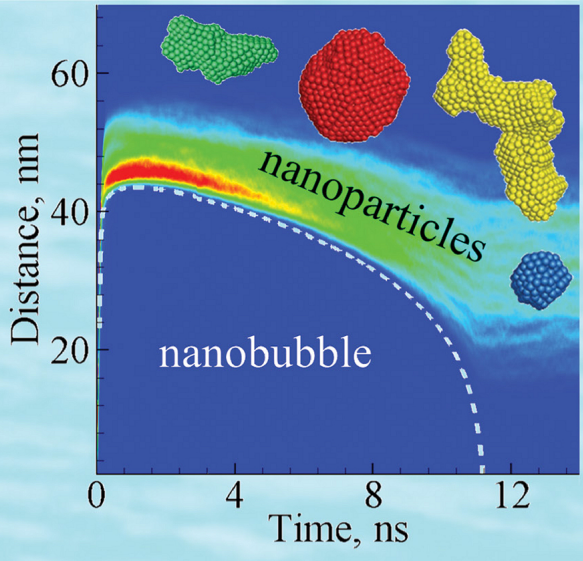

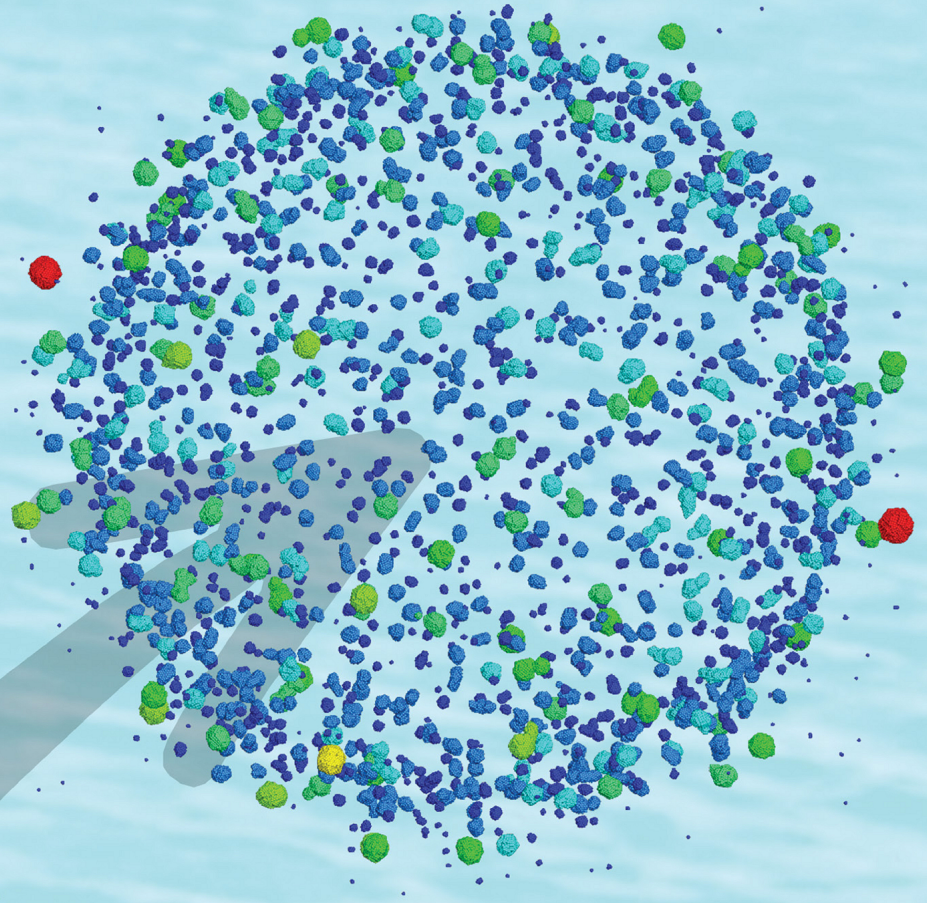

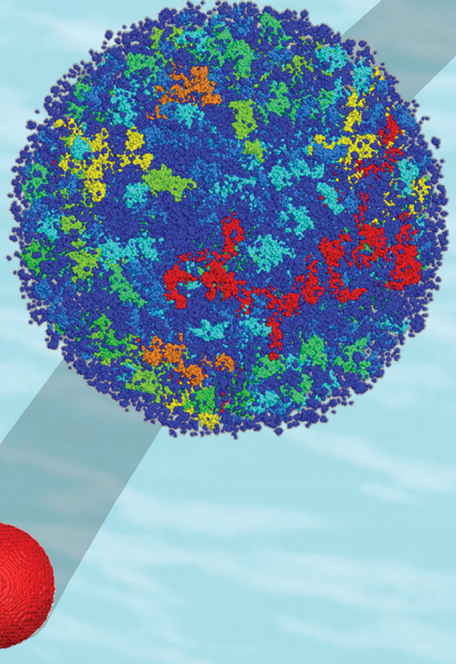

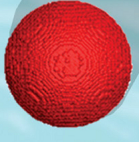

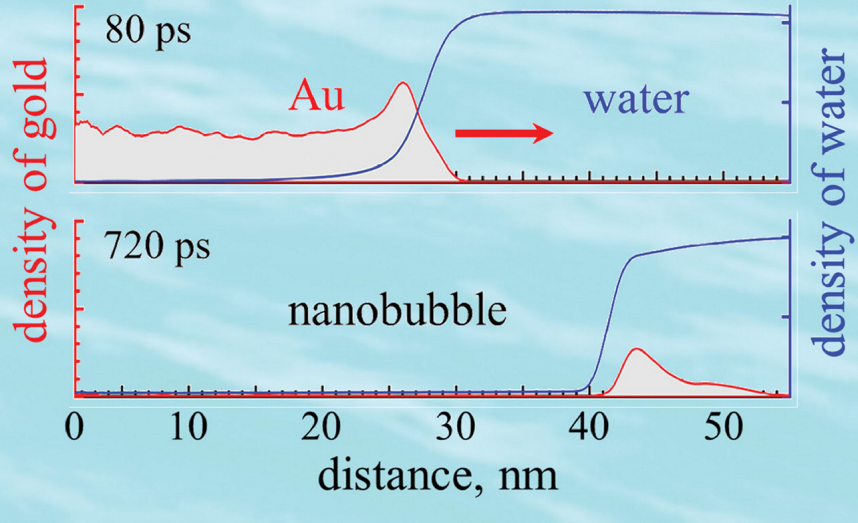

ACS Publications
Most Trusted. Most Cited. Most Read.

www.acs.org

THE JOURNAL OF PHYSICAL CHEMISTRY C
A JOURNAL OF THE AMERICAN CHEMICAL SOCIETY

pubs.acs.org/JPCC

Article

Atomistic View of Laser Fragmentation of Gold Nanoparticles in a Liquid Environment

Hao Huang and Leonid V. Zhigilei*

Cite This: J. Phys. Chem. C 2021, 125, 13413−13432

Read Online

ACCESS | Metrics & More | Article Recommendations | Supporting Information

ABSTRACT: Short-pulse laser irradiation of a colloidal solution of nanoparticles is an effective method for fragmenting the nanoparticles and producing a population of smaller nanoparticles and atomic clusters with properties desired in various fields of applications, including biology, medicine, and catalysis. To investigate the mechanisms involved in the fragmentation, we develop a computational model capable of realistic treatment of a variety of interrelated processes occurring on different time and length scales, from the electronic excitation by the laser pulse, to the electron−phonon energy transfer and an explosive phase decomposition of the superheated nanoparticle, and to the generation and collapse of a nanobubble in a liquid environment. The application of the model to simulation of laser fragmentation of a Au nanoparticle in water has revealed two distinct channels of the formation of the fragmentation products. The first channel involves the direct injection of compact nanodroplets propelled by the phase explosion of the irradiated nanoparticle deep into the water environment. The second channel of the nanoparticle formation involves a more gradual growth through agglomeration of numerous atomic clusters embedded into a narrow region of water surrounding the laser-induced nanobubble. This channel produces irregularly shaped nanoparticles and leads to a rapid decline of the population of atomic clusters on the timescale of nanoseconds. All the clusters and nanoparticles experience an ultrafast quenching by the water environment and feature a high density of twin boundaries and other crystal defects, which may enhance the density of active sites for the catalytic applications of the nanoparticles. The computational predictions of the prompt generation of a high concentration of the fragmentation products in a relatively narrow shell-like region on the outer side of the nanobubble, as well as the rapid solidification of atomic clusters and nanoparticles at the early stage of the nanobubble formation, have important practical implications for the design of new methods aimed at achieving an improved control over the size, shape, and defect structures of nanoparticles produced by laser fragmentation in liquids.

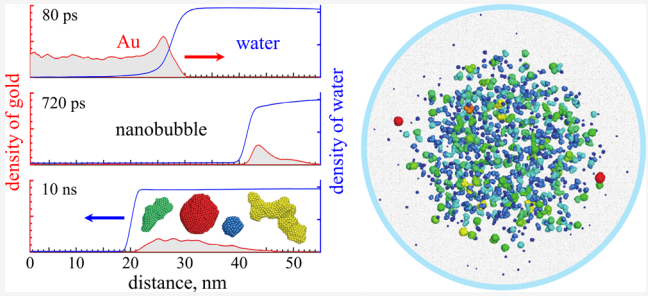

1. INTRODUCTION

Laser interaction with absorbing nanoparticles in liquids is in the core of several current and emerging applications, including the selective killing of cancer cells,[1−3] biological imaging,[4,5] drug delivery,[6,7] and laser processing of colloidal solutions of nanoparticles.[8−25] The latter includes laser fragmentation in liquid (LFL),[16−25] where larger nanoparticles are fragmented to produce a population of smaller nanoparticles with a narrow size distribution, and laser melting in liquid,[11−15] where melting and partial vaporization of nanoparticles is used to change the size,[11,12] shape,[13,14] and composition[15] of the colloidal nanoparticles.

The relevance of the laser interaction with nanoparticles in liquids to a broad range of practical applications has stimulated experimental and theoretical efforts aimed at revealing the cascade of processes triggered by the laser energy deposition and responsible for the nanoparticle modification and energy transfer to the liquid environment. In many experimental studies, the mechanistic information is inferred from the results of postprocessing analysis of the outcomes of the laser irradiation, such as the cell lethality and cell membrane permeability in biomedical applications[1−3,6,7] or changes in nanoparticle shapes and size distributions in laser melting and fragmentation experiments.[11−13,15,16,18−20] The time-resolved optical[14,21,26−28] and X-ray scattering[14,25,29,30] measurements have provided valuable insights into the characteristic time-scales of the expansion and collapse of nanobubbles generated around the irradiated nanoparticles,[25,27−30] the nanoparticle temperature evolution,[14,26] and the nanoparticle fragmentation dynamics.[21,25] Moreover, recent synchrotron X-ray scattering experiments were used to directly probe the structural changes

Received: April 7, 2021
Revised: May 25, 2021
Published: June 9, 2021

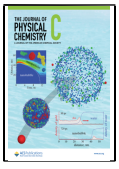

in the irradiated nanoparticles (thermal expansion, melting, and recrystallization) with sub-nanosecond time resolution.[25]

The advances in the experimental probing call for concurrent progress in theoretical interpretation and modeling, which has been hampered by the dynamic, highly nonequilibrium nature of processes induced by the rapid laser energy deposition. The challenges exist even in the irradiation regime where the nanoparticles survive the irradiation and retain their integrity. The large mismatch in thermophysical properties of nanoparticles and the surrounding liquid can produce large thermal resistance at the nanoparticle−liquid interface, which may lead to a substantial temperature drop at the interface.[30−34] Moreover, the explosive boiling[35] of strongly superheated liquid surrounding a hot nanoparticle can lead to the formation of a vapor bubble that further slows down the nanoparticle cooling process.[36−39] For small vapor bubbles surrounding the nanoparticles, the thermal energy transport through the bubble cannot be described by the Fourier law, and the ballistic heat transfer mechanism should be considered for a realistic description of the bubble dynamics.[39] For very small nanoparticles with diameters of just a few nanometers, the bubble formation can be suppressed by a high curvature of the nanoparticle−liquid interface,[33,34] thus sustaining high interfacial heat fluxes and leading to extreme cooling rates experienced by the nanoparticles, as demonstrated in molecular dynamics (MD) simulations of nanoparticles rapidly heated in a liquid environment[40] or injected into liquid in the course of laser ablation.[41−43] While the specifics of the nanoscale heat and mass transfer around a nanoparticle excited by a laser pulse can be, to a certain extent, incorporated into the general framework of hydrodynamic modeling based on an equilibrium equation of state of the liquid environment,[37,38,44−47] the full account for the interplay of various channels of the laser energy redistribution is still challenging to achieve.

The transition to the nanoparticle fragmentation regime brings the complexity of the theoretical treatment of the problem to the next level and largely limits the interpretation of experimental results to the semiquantitative evaluation of possible processes.[22,48−50] In general, the fragmentation mechanisms discussed in the literature can be separated into photothermal, photomechanical, and electrostatic ones, although more exotic mechanisms, such as nonthermal ion emission from solid nanoparticles driven by an electric field of a high-intensity femtosecond laser pulse locally amplified through polarization of the nanoparticle,[51] have also been suggested.

The discussion of the *photothermal mechanism* of nanoparticle fragmentation is usually based on estimation of the temperature rise in response to the laser excitation.[16,18,20−22,48−50,52] The sequential heating, melting, and evaporation of irradiated nanoparticles at moderate laser fluences can reduce the size of the primary nanoparticles and lead to the appearance of a new population of smaller ones through the nucleation and growth from the evaporated atoms. At higher fluences, the nanoparticles can be completely evaporated or undergo an explosive decomposition into vapor and liquid droplets when superheated up to the limit of thermodynamic stability of the molten material (close to a spinodal temperature).[53−56] Indeed, the observations of bimodal size distributions of Au nanoparticles in both picosecond[18,25] and nanosecond[23,24] LFL experiments, as well as the disappearance of the population of large nanoparticles with increasing laser fluence[18,23,24] and number of pulses,[18] are consistent with this fragmentation pathway.

The *photomechanical mechanism* of nanoparticle fragmentation can be activated under conditions of stress confinement,[57,58] when the time of the laser heating (defined by the laser pulse duration, τ_p, or the time of the electron−phonon equilibration, $\tau_{e\text{-}ph}$, whichever is longer) is shorter than the time required for the mechanical relaxation (expansion) of the nanoparticle, that is, $max\{\tau_p, \tau_{e\text{-}ph}\} \leq R/C_s$, where C_s is the speed of sound and R is the radius of the nanoparticle. With $\tau_{e\text{-}ph} \approx 10$ ps[59] and $C_s \approx 3240$ m/s for Au, the stress confinement condition is satisfied for nanoparticles with diameters larger than ∼60 nm when $\tau_p \leq 10$ ps. The dynamic relaxation of the compressive stresses generated under stress confinement can lead to mechanical damage or disintegration of nanoparticles.[60,61] While the solid-state photomechanical disintegration is highly unlikely for metal nanoparticles, the photomechanical effects can make a substantial contribution to the nanoparticle disintegration above the melting threshold.[50,62]

Finally, the possibility of the *electrostatic mechanism* of nanoparticle fragmentation[22,50,63] driven by the Coulomb instability/explosion of nanoparticles strongly ionized due to a massive thermionic and/or photoelectric electron emission has also been discussed for femtosecond,[21] picosecond,[20] and nanosecond[64] pulse LFL. We note that a simple criterion for the onset of the Coulomb explosion formulated in terms of a threshold electron temperature at which the number of electrons with thermal energy exceeding the work function reaches a critical level[21,22,50,63] should be considered with caution. The accumulation of the positive charge should increase the effective work function and eventually prevent further ionization.[20] Moreover, the emitted electrons can be expected to be trapped within ∼10 nm water shell around the nanoparticle,[65] thus creating a negative space charge and further reducing the number of emitted electrons.[66,67] Thus, a reliable analysis of the electrostatic fragmentation at the limit of stability for multiply charged particles should involve a self-consistent evaluation of the electron emission and the electric field,[66−68] as well as the effect of the liquid environment on the charge distribution and screening.

The irradiation regimes where the thermal, mechanical, and electrostatic processes contribute to the nanoparticle fragmentation in LFL are likely to overlap, and these contributions may be intertwined with each other. As discussed above, the complexity of the processes makes simple estimations based on the energy balance unreliable and calls for a more detailed analysis. Ideally, the theory and computational modeling should predict time-resolved thermodynamic and structural information that can be directly verified in advanced optical and X-ray probing of the nanoparticle fragmentation dynamics.[14,21,25]

As a step in this direction, in the present paper, we report the development of a model suitable for detailed analysis of the dynamics of photothermal and photomechanical nanoparticle fragmentation on the timescales of the expansion and collapse of a nanobubble generated around the irradiated nanoparticle. We then put the model to test by performing a simulation of fragmentation of a gold nanoparticle irradiated by a 10 ps laser pulse in the regime comparable to that used in a recent experimental study,[25] which provides the most complete information on the LFL process to date by combining *ex situ* analysis of the fragmentation products with *in situ* X-ray

https://doi.org/10.1021/acs.jpcc.1c03146
J. Phys. Chem. C 2021, 125, 13413−13432

probing of the fragmentation dynamics. The computational predictions on the nanobubble lifetime and the final size distribution of small nanoparticles produced by LFL are in good quantitative agreement with experimental observations. The simulations explain the observation of a prompt (nearly instantaneous) formation of a large number of atomic clusters and small nanoparticles with diameters less than 4 nm. Most of these clusters are generated just outside the boundaries of the nanobubble during the first nanoseconds after the laser pulse, long before the bubble collapse at ∼11 ns. Moreover, even though the simulation is performed for conditions when the laser excitation supplies more than 80% of the energy required for complete vaporization of the nanoparticle, some of the fragments undergo crystallization as early as 0.3 ns after the laser pulse. The intriguing computational prediction of the rapid crystallization occurring within the nanobubble's outer layer, prior to the nanobubble collapse, presents a new challenge for the time-resolved X-ray or electron diffraction probing.

2. COMPUTATIONAL MODEL FOR LFL

The simulation of laser fragmentation of a gold nanoparticle in a liquid environment is performed with a computational model combining a fully atomistic description of laser interaction with the gold nanoparticle,[69,70] a coarse-grained (CG) representation of liquid (parameterized for water),[41,42,71,72] and an acoustic impedance matching boundary condition[73−75] designed to mimic the nonreflecting propagation of the laser-induced spherical pressure wave through the boundary of the computational domain. An important new feature of the model is the implementation of an on-the-fly cluster analysis that enables a realistic description of the size dependence of the electron−phonon coupling coefficient and a detailed tracking of the mechanisms of the nanoparticle generation in LFL. A schematic representation of the computational system is shown in Figure 1. A description of the main components of the model and details of the computational setup are provided below.

2.1. TTM-MD Model for Laser Fragmentation of Nanoparticles. The laser interaction with a gold nanoparticle is simulated with a hybrid atomistic-continuum model that combines the atomistic MD method[76,77] with a continuum description of laser excitation of conduction-band electrons, followed by electron−phonon equilibration based on the two-temperature model (TTM).[78] Since the combined TTM-MD model has been described in detail in previous publications,[42,69,70] here, we only describe the changes introduced into the model to enable the simulation of laser-induced fragmentation of nanoparticles in a liquid environment.

In the conventional formulation of the TTM-MD model,[69,70] the heat diffusion equation for the electron temperature, T_e, is solved by a finite difference method simultaneously with MD integration of the equations of motion of atoms. The cells in the finite difference discretization are related to the corresponding volumes of the MD system, and the local lattice temperature,[79] T_l, is calculated for each cell from the average kinetic energy of thermal motion of atoms. The energy exchange between the electrons and atomic vibrations is then defined by the instantaneous local values of T_e and T_l. The energy exchange is realized by adding special coupling terms to the MD equations of motion and the differential equation for T_e. In the applications of the TTM-MD model to laser interactions with bulk metal targets and thin films, the uniaxial expansion of an irradiated target is treated in an ad hoc manner by activating the new cells when material moves in, accounting for atoms in deactivated cells by including them into the nearest active cells, and moving the electron thermal energy from cell to cell together with the atoms. This treatment provides a realistic description of various channels of laser energy redistribution and ensures the total (electrons plus atoms) energy conservation during the simulations.[69,80]

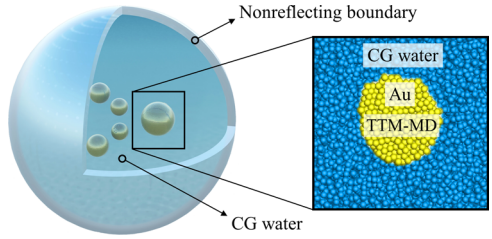

Figure 1. Schematic representation of the computational setup used for simulation of laser fragmentation of a gold nanoparticle in water. The initial colloidal nanoparticle is in the center of a spherical computational domain and is surrounded by liquid. The laser interaction with the initial nanoparticle leading to its fragmentation is simulated with an atomistic TTM-MD model. On-the-fly cluster analysis is implemented in the TTM-MD model to account for the size dependence of the electron−phonon coupling coefficient. The liquid surrounding the nanoparticle is represented by a coarse-grained MD model (CG water), with the thickness of the CG water shell chosen to ensure that all laser-induced fragmentation products remain within the computational domain during the simulation. The nonreflecting propagation of the laser-induced spherical pressure wave from the computational domain to the surrounding water environment is represented by the acoustic impedance matching boundary condition applied to the outer shell that changes its radius during the simulation. A zoom-in view of one of the nanoparticle fragments is provided on the right side of the figure.

In the case of LFL, however, the rapid fragmentation of irradiated nanoparticles and three-dimensional expansion of fragmentation products (small nanoparticles, atomic clusters, and individual atoms) makes the conventional TTM-MD approach described above unsuitable. The fragmentation induced by an ultrashort laser pulse can occur before the complete electron−phonon equilibration, making it necessary to determine T_e and T_l for individual fragments. An attempt to map the fragmentation products to a regular grid of cubic cells produces the number of atoms per cell that is too small for a reliable calculation of T_l, which requires discrimination between the thermal kinetic energy and the energy of the center-of-mass motion of the atomic clusters and small nanoparticles. While dividing the space into spherical shells instead of the cubic cells eliminates the statistical noise in the collective radial velocity and temperature averaged over all atoms located within the same shell, this approach also introduces severe artifacts into the simulation results. In particular, an assumption that all clusters and nanoparticles in the same shell have a common electron temperature creates an artificial channel for the heat transfer within the shell when clusters and nanoparticles with $T_l > T_e$ effectively transfer energy to the ones with $T_l < T_e$ through the electron−phonon coupling.

Given the inability of approaches based on the partitioning of space into cells to provide an adequate description of the electron−phonon equilibration in a nanoparticle undergoing laser-induced fragmentation, we designed an alternative

https://doi.org/10.1021/acs.jpcc.1c03146
J. Phys. Chem. C 2021, 125, 13413−13432

approach based on continuous identification of the size (characterized by the number of atoms N) of all particles in the course of a TTM-MD simulation. The key component of this approach is a computationally efficient cluster analysis algorithm described in Section 2.3. The algorithm enables rapid on-the-fly identification of atomic clusters, defined as particles with equivalent diameter D_e[81] of less than 2.2 nm ($N < 333$),[82] and nanoparticles, defined as particles with $D_e \geq 2.2$ nm ($N \geq 333$), at any time step during the simulation.

All atoms that belong to the same particle (cluster or nanoparticle) share the same T_e and T_l. The lattice temperature T_l is calculated from the kinetic energy of atomic motion in the particle center-of-mass frame of reference. For small atomic clusters consisting of fewer than 56 atoms, the internal temperature cannot be reliably defined, but it is still calculated from kinetic energy (without subtraction of the center-of-mass velocity) and used to formally define the transfer of the residual excess electron energy remaining in the clusters generated by LFL to the energy of atomic motions (see Section 2.2).

Similar to the conventional TTM-MD,[69,70] the electron energy is carried along by atoms that are leaving or joining a particle. For example, when an atom evaporates from a particle, it retains the electron energy that corresponds to T_e of the particle. When two clusters or nanoparticles merge together, their electron energy is combined, and a new T_e is calculated. Since all of the nanoparticle fragments are much smaller than the electron mean free path in Au,[83] the establishment of the common electron temperature is considered to be instantaneous, and the electron thermal conductivity term is omitted in the TTM equation for T_e. The electron heat capacity, used in the calculation of the electron energy and in the TTM equation for T_e, is taken in the form that accounts for the thermal excitation from the electron states below the Fermi level.[84]

The small size of the nanoparticle fragments not only eliminates the need for an explicit treatment of the electron thermal conductivity but also makes it necessary to consider the effect of the small size of the nanoparticles[85−91] and atomic clusters[92−98] on the rate of the energy exchange between the excited electrons and the thermal energy of atomic vibrations. In the approach where the electron−phonon coupling is implemented on the particle-by-particle basis, the size dependence of the electron−phonon coupling can be readily introduced into the model, as described in the next subsection.

2.2. Size Dependence of Electron−Phonon Coupling in Metal Nanoparticles. The dependence of the characteristic time of the electron−phonon equilibration on the nanoparticle size has been consistently observed in time-resolved pump−probe spectroscopy measurements performed for sufficiently small Sn,[85] Ga,[86] Cu,[89,91] Ag,[87,88,91] and Au[88,91,97] nanoparticles. These observations have been attributed to coupling of the excited electrons to surface vibrational modes[85−87,89] that can be enhanced by extra scattering or trapping of the excited electrons by surface imperfections[89] and by the decrease of screening of the electron−ion interaction close to the surface due to the reduction of the density of conduction electrons ("spill-out" of electron wave functions).[88,90,91] The experimental data suggest that a hypothetical opposing effect related to the decreasing overlap between the electron oscillation frequencies (increasing with size reduction) and the phonon frequencies[99] plays a secondary role and is overshadowed by the contribution of surface scattering.[92]

For Au, a substantial increase in the electron−phonon energy exchange rate is reported for nanoparticles smaller than 10 nm in a study probing the nanoparticles in a size range of 2.2 to 20 nm.[88,91] This trend is confirmed in more recent measurements performed for atomically precise gold nanoparticles,[97] where the electron−phonon equilibration time in the low-excitation limit is observed to decrease as the size of the Au nanoparticles decreases from 13 to 3.5 nm and to 2.9 nm. When the results for larger 9, 22, and 48 nm nanoparticles are compared,[100] however, no significant size dependence of the electron−phonon thermalization time is observed. Similarly, no size dependence of the effective strength of electron−phonon coupling was observed for Au nanoparticles with sizes ranging from 20 to 83 nm, while an increase of the coupling strength by up to a factor of 2 is measured for hollow Au nanoshells with similar diameters but shell thicknesses ranging from 5.7 to 10 nm.[101] These observations, and an apparent linear correlation of the increase of the electron−phonon coupling strength with the surface-to-volume ratio in the hollow nanoshells, support the role of the surface scattering in the electron−phonon coupling enhancement and suggest the onset of a pronounced size dependence in Au nanostructures of dimensions that are less than 10 nm.

As the diameter of Au nanoparticles decreases below ∼2.5 nm, the electronic structure transforms from a metallic to discrete molecular type, as manifested by the disappearance of surface plasmon resonance in the absorption spectrum.[93] A detailed analysis of the evolution from metallic to molecular state in thiolate-protected Au clusters/nanoparticles consisting of 25 to 940 atoms (D_e from 0.9 to 3.1 nm) has identified a transition from the metallic (plasmonic) to molecular-like (excitonic) state in a size range from 144 to 333 atoms (1.7−2.2 nm).[97] For particles larger than 2.2 nm, the electron−phonon coupling time determined in transient absorption spectroscopy experiments is found to increase with the pump laser fluence, as expected from the linear dependence of the electron heat capacity in metallic nanoparticles.[102] The fluence dependence measured for 2.2 nm (333 atoms) nanoparticles, however, is rather weak and is not observed for 144 atom clusters (D_e = 1.7 nm). The absence of the fluence dependence of the electron−phonon relaxation time for 1.7 nm clusters is an evidence of the emergence of discrete electron energy states and single-electron excitation dynamics,[94] while the weakening of the dependence for 2.2 nm nanoparticles indicates a transitional state between the metallic and molecular behavior.[97]

The transition from the electron−phonon coupling in metallic nanoparticles to the electron−hole recombination in atomic clusters is usually associated with a slowdown of the relaxation of the excited electrons. In particular, in ref 97, a steady decrease of the electron−phonon relaxation time down to less than 1 ps, observed as the size of Au nanoparticles is reduced from 13 nm down to 2.6 nm (∼520 atoms), turns into an increase to 1.6 ps for 333-atom clusters and to 3 ps for 144-atom clusters. A similar trend is reported in ref 95, where the excited-state decay rate increases when the size of the Au nanoparticle is decreased from 3 to 2.2 nm but decreases when the size is further reduced to 1.7 and 1.1 nm. The relaxation of optically excited electronic states in atomic clusters clearly reflects the presence of discrete electron energy states and is characterized by multiple relaxation channels ranging from

https://doi.org/10.1021/acs.jpcc.1c03146
J. Phys. Chem. C 2021, 125, 13413−13432

slow nano-/microsecond radiative and nonradiative relaxation of lowest electronic excited states to ultrafast sub-picosecond relaxation of higher excited states.[92−98] Moreover, the excited-state lifetimes can be substantially affected by ligands attached to the Au clusters.[94,96,103,104]

Based on the brief overview of the current understanding of the nanoparticle/cluster size dependence of the relaxation of excited electronic states provided above, we adopted the following simplified description of the energy exchange between the electrons and thermal atomic motion in the metal particles. The general description of the energy exchange is the same for nanoparticles and clusters of all sizes and is based on the conventional TTM-MD approach,[42,69,70] where the electron−phonon coupling terms are added to the MD equations of motion and to the TTM equation for T_e applied at the level of individual particles, as described in Section 2.1. The rate of the energy exchange in a given particle is defined by the difference between T_e and T_l determined for the particle, as well as the magnitude of the electron−phonon coupling factor $G_p(T_e, D_e)$ that depends on the electron temperature T_e and the size of the particle D_e. The electron temperature and size dependence is approximated as $G_p(T_e, D_e) = \alpha(D_e)G_{bulk}(T_e)$, where $G_{bulk}(T_e)$ is the electron−phonon coupling factor of a bulk metal and $\alpha(D_e)$ is the size-dependent scaling coefficient. The electron temperature dependence of the electron−phonon coupling factor, $G_{bulk}(T_e)$, is taken in the form[84,105] that accounts for the contribution of d band electrons that can be thermally excited in Au at $T_e > 3000$ K, while the scaling coefficient $\alpha(D_e)$ is shown in Figure 2 and explained below.

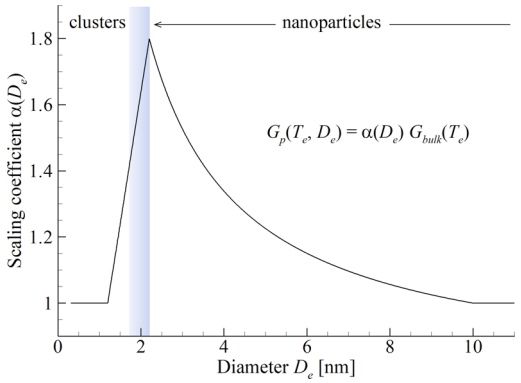

Figure 2. Scaling coefficient $\alpha(D_e)$ used for an approximate representation of the dependence of the electron−phonon coupling factor on the Au nanoparticle/cluster diameter D_e. The shaded area marks the particle size range that corresponds to the transition between the metallic (plasmonic) and molecular (discrete/excitonic) type of the electronic structure.

For Au nanoparticles larger than 10 nm, the experimental data do not reveal any significant size dependence of the electron−phonon equilibration time,[88,91,100,101] and the electron−phonon coupling factor of a bulk metal is assumed, that is, $\alpha(D_e) = 1$ and $G_p(T_e, D_e) = G_{bulk}(T_e)$ for nanoparticles with $D_e \geq 10$ nm (more than 31,180 atoms).

For smaller nanoparticles, in the size range 2.2 nm < D_e < 10 nm, the increase in the rate of the electron−phonon equilibration with decreasing size of the nanoparticles[88,91,97] is accounted for by the size-dependent scaling coefficient $\alpha(D_e)$ fitted to the linear dependence of the experimental electron−phonon energy transfer rate on inverse particle diameter reported in ref 91. The fitting yields $\alpha(D_e) = A/D_e + B$, where $A = 2.2564$ nm and $B = 0.7744$. Note that the functional form of the size dependence is consistent with that expected from the contribution of surface scattering to the electronic relaxation in nanoparticles.[92,106]

For the atomic clusters[82] with D_e < 2.2 nm, the transition from the metallic to molecular type of the electronic structure leads to the emergence of multiple decay rates corresponding to different steps of the excited-state relaxation, which are sensitive to the electronic and nuclear relaxation dynamics, capping by ligands, interaction with the environment, and level of excitation.[92−98] Strictly speaking, the concept of the electron−phonon coupling is not applicable to the atomic clusters, but it can still be used in the model to represent the effect of radiationless relaxation of excited electronic states through internal conversion and vibrational cooling. Based on the evidence that the rate of the relaxation of electronic excitation turns from increase to decrease when D_e is reduced below ∼2.2 nm,[95,97] we reduce $\alpha(D_e)$ linearly between 2.2 and 1.2 nm, from α(2.2 nm) to α(1.2 nm) = 1, and keep the electron−phonon coupling factor at a constant level that corresponds to the bulk metal for smaller clusters with D_e < 1.2 nm (less than 54 atoms).

We note that the rough assumptions made for atomic clusters smaller than 2.2 nm (both the simplified size dependence and the bulk-like electron temperature dependence) are not intended to reflect the complexity of real electronic relaxation in small atomic clusters, where the sensitivity to the level of excitation, atomic structure, and environment can lead to the variation of the relaxation timescales by a few orders of magnitude.[92−98] Rather, these assumptions are made to simplify the computational treatment of the residual excess electron energy remaining in small clusters generated in LFL. Due to the small amount of this residual energy, the results of the LFL simulations are not sensitive to the choice of approximations used for the description of the electron relaxation in the small atomic clusters. We note, however, that the general framework of the model developed in this work makes it possible to introduce a more fine-grained and precise description of the relaxation of the excited electronic states, if needed, for example, for making connections to time-resolved optical emission measurements.

The effect of the environment of nanoparticles on the internal electron thermalization is not yet fully established[90] but appears to be moderate[101,103] or absent[88] for nanoparticles with D_e > 2.2 nm. Therefore, in the current parametrization of the model, we do not account for the possible effect of the surroundings on the electron−phonon coupling. We also do not incorporate the effect of melting of the nanoparticles on the strength of the electron−phonon coupling. The experimental data on the electron−phonon coupling in molten metals are scarce, although the results for solid and liquid metallic gallium nanoparticles with diameters of ∼10 to 18 nm embedded in a SiO matrix reveal similar dynamics of the electron energy relaxation in both phases.[86] Recent theoretical calculations for solid and liquid Al also suggest a weak effect of the structural disorder on the strength of the electron−phonon coupling.[107] We note, however, that the effects of the environment, the internal crystal defects,[108,109] and the phase state of the nanoparticles can be readily introduced into the model once reliable experimental data and/or theoretical predictions on these effects are available.

https://doi.org/10.1021/acs.jpcc.1c03146
J. Phys. Chem. C 2021, 125, 13413−13432

2.3. On-the-Fly Parallel Cluster Analysis Algorithm.

The computational model described above involves a particle-by-particle treatment of the electron−phonon equilibration and, therefore, requires real-time ("on-the-fly") identification of all atomic clusters and nanoparticles in the course of the simulation. In this section, we describe a simple yet computationally efficient cluster identification algorithm incorporated into the model. The algorithm takes advantage of the list of neighbors of each atom constructed for the treatment of interatomic interactions using the cell-linked list method.[110] The cluster analysis is first performed at the level of individual processors and then extended to the whole system simulated with a parallel code.

The single-processor (serial) cluster analysis algorithm consists of four steps illustrated in Figure 3. In the first step,

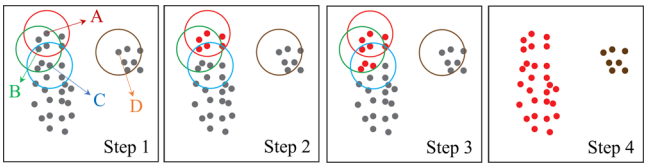

Figure 3. Schematic of a series of steps in the serial cluster analysis algorithm. Atoms without cluster ID are colored gray. Atoms assigned different cluster IDs are colored by different colors.

for each atom in a part of the system treated by a given processor, a list of atoms that are within the cutoff distance used for defining whether the two atoms belong to the same cluster is generated. These lists are produced based on the lists of neighbors used for the description of interatomic interactions in the MD simulation code. The circles drawn around atoms A, B, C, and D have the same radius equal to the cluster cutoff distance and encircle the atoms that are assigned as neighbors of these four atoms. In the second step, we pick one atom (e.g., atom A) and assign all its neighbor atoms with the same cluster ID. In the third step, we systematically go through all the neighbors of atom A (e.g., atom B) and assign their neighbors the same cluster ID. The process is repeated for all the neighbors of neighbors of atom A (e.g., atom C) and so forth, until all the chains of the ID assignment triggered by atom A are exhausted. In the fourth step, the next atom that has not been assigned a cluster ID yet is selected, a new cluster ID is generated (see below) and assigned to this atom, and the process described above for steps 2 and 3 is repeated. The steps 4-2-3 are repeated until all the atoms in the part of the system treated by the processor are assigned with cluster IDs.

The extension of this algorithm to analysis of a large computational system simulated by a parallel TTM-MD code requires additional steps. The parallel code splits the system into regions treated by different processes, and some of the clusters can span over two or more regions. Therefore, the cluster identification algorithm should combine different parts of the same cluster identified by different processors into a single cluster. This is accomplished through a series of steps illustrated in Figure 4. In the two-dimensional (2D) schematic of a three-dimensional (3D) partitioning of the system between the processors, shown in this figure, the system is divided into nine squares, with each square treated by one processor. As the first step of cluster identification in the parallel algorithm, each processor performs cluster analysis on local atoms, as described above and is illustrated in Figure 3. The assignment of cluster IDs is based on the minimum global

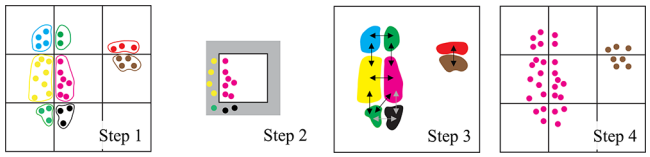

Figure 4. Schematic of the on-the-fly parallel cluster analysis algorithm. Each square represents a region treated by a single processor. Atoms are colored by the cluster IDs. The gray region in step 2 is a skin layer where the atoms sent by neighboring processors are located. Colored areas in step 3 show different parts of clusters joined together by the master processor. Arrows in step 3 show the pairs of local clusters identified in step 2.

atom ID out of all atoms that belong to the cluster. This assignment of cluster IDs ensures that all cluster IDs in all processors are unique. The atoms in Figure 4 are colored by these unique cluster IDs after the first step.

Next, each processor sends information about atoms located in a buffer layer at the periphery of its region to other processors responsible for the adjacent neighboring regions. The atoms received from adjacent processors are located within the skin layer surrounding each single-processor region. A skin layer is shown schematically as a gray layer in step 2 of Figure 4. Using the list of neighbors, a check is performed on whether any of the atoms in the skin layer should be included into the clusters identified earlier by the local processor. When such atoms are found, the pairs of cluster IDs to be joined are identified. In the third step, each processor sends the pairs of cluster IDs to the master processor. The master processor applies the cluster analysis again, but this time to the parts of the clusters identified by cluster IDs, and combines the cluster parts into joint clusters. As a result, the parts of a cluster located in regions that are distant from each other (e.g., in the top left and bottom left regions in Figure 4) become parts of the same cluster. In the final step, the master processor sends both the old and new cluster IDs to the local processors. Each processor updates the cluster ID and cluster size for every atom, and this information is used in defining the behavior of the atoms (strength of electron−phonon coupling, Section 2.2) and in the analysis of atomic configurations.

2.4. Computational Setup and Parameters.

As the first application of the new model, we perform a simulation of LFL of a 20 nm Au nanoparticle irradiated by a laser pulse with a Gaussian temporal profile and a full width at half maximum duration of 10 ps. To ensure the complete energy deposition, the time when the pulse reaches its peak power is shifted with respect to the start of the simulation by 25 ps. The total energy density supplied by the laser pulse is 3.6 eV/atom. This energy density corresponds to around 94% of the cohesive energy of Au (3.81 eV/atom)[111] and around 80% of the energy required for complete vaporization of the nanoparticle. The latter is estimated by summing the energy density needed to heat bulk Au from 300 K to the melting temperature of T_m = 1337 K (29.0 kJ/mol = 0.3 eV/atom), melt it (enthalpy of melting H_m = 12.6 kJ/mol = 0.13 eV/atom), heat molten Au from T_m to the boiling temperature of T_b = 3130 K (55.5 kJ/mol = 0.58 eV/atom), and completely vaporize it at T_b (334.4 kJ/mol = 3.47 eV/atom), yielding a total of 4.48 eV/atom. The surface energy of a 20 nm nanoparticle does not significantly contribute to the overall energy balance, as can be estimated using experimental surface energy of solid and liquid Au,[112] 1.41 and 1.14 J/m^2, respectively, yielding the contribution of

https://doi.org/10.1021/acs.jpcc.1c03146
J. Phys. Chem. C 2021, 125, 13413−13432

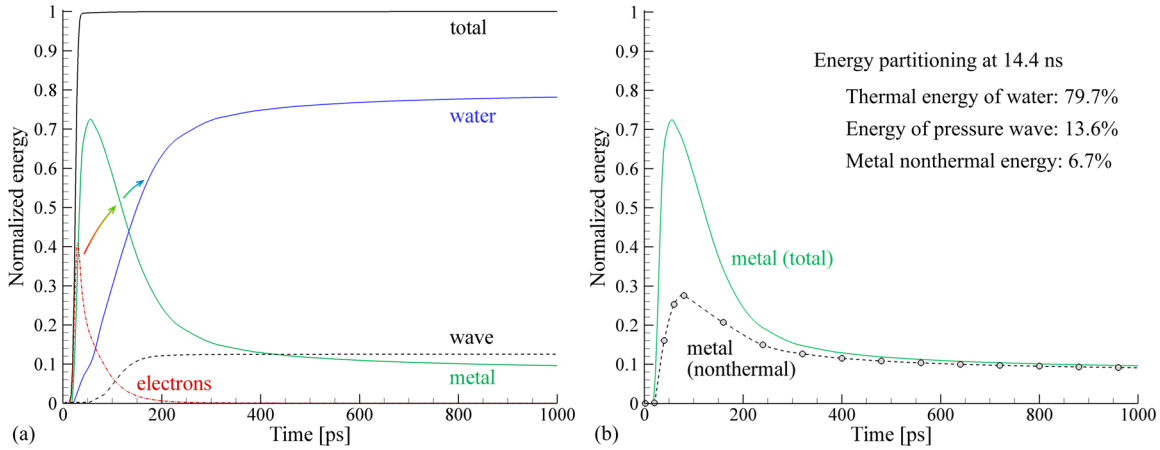

Figure 5. Redistribution of the deposited laser energy in a simulation of LFL of a 20 nm Au nanoparticle irradiated by a 10 ps laser pulse that deposits the total energy density of 3.6 eV/atom. The energy of the excited electrons (red dash-dotted line), metal atoms (solid green line), and water (solid blue line), along with the energy removed from the computational domain by the outgoing spherical pressure wave (black dashed line) and the total energy deposited by the laser pulse (solid black line), are shown in (a). The nonthermal part of the metal atoms' energy (mostly the energy of new surfaces produced by the fragmentation of the initial nanoparticle) is also shown in (b) by the dashed black line connecting the data points. All energy contributions are shown relative to the initial values in the 20 nm Au nanoparticle−water system equilibrated at 300 K and are normalized by the total energy absorbed by the nanoparticle. The arrows in (a) schematically show the dominant channel of the energy redistribution from the excited electrons to the energy of Au atoms and to the thermal energy of the water environment.

~0.04 eV/atom to the energy of the nanoparticle. The choice of the deposited energy density is motivated by the recent experimental study,[25] where a detailed time-resolved probing of the LFL process is reported for a laser fluence just below the threshold for complete nanoparticle vaporization. One notable difference from the experimental study is that the size of the nanoparticle in the simulation is reduced by more than a factor of 2 with respect to the 54 nm nanoparticles used in the experiments in order to keep the computational cost of the simulation at a reasonable level.

The laser fluence that corresponds to the deposited energy density assumed in the simulation is estimated using the Mie theory calculations performed with MiePlot.[113] The calculations yield the absorption efficiency (ratio of the absorption cross section to the particle cross section) of 1.228 for a 20 nm Au nanoparticle irradiated at a wavelength of 532 nm in water, close to the value reported in ref 114. With this absorption efficiency, the absorbed energy density of 3.6 eV/atom corresponds to a fluence of 360 J/m^2 for irradiation at a wavelength of 532 nm. We note, however, that direct conversion of the incident laser fluence to the absorbed energy density based on the Mie theory calculations may result in a significant (by more than a factor of ~4)[115] overestimation of the latter in the regime of nanobubble formation, nanoparticle melting,[30] and fragmentation.[25] This overestimation can only partially be attributed to the transient plasmon band bleaching in the electronically excited nanoparticles[116] and requires further analysis.

The initial Au nanoparticle has a diameter of around 20 nm and consists of 240,591 atoms. As discussed in Section 2.1 and illustrated in Figure 1, the laser interaction with the Au nanoparticle is simulated with the TTM-MD model modified to include a particle-by-particle treatment of the electron−phonon equilibration. The interatomic interactions in the MD part of the TTM-MD model are described by the embedded atom method (EAM) potential with parametrization suggested in ref 117. The potential predicts a melting temperature of 1330 K, which is close to the experimental value of 1337 K, and reproduces the experimental heat of melting of 0.13 eV/atom.

The water surrounding the Au nanoparticle is represented by a combination of a CG MD model[41,42,71,72] with an acoustic impedance matching boundary condition[73−75] parameterized to simulate a nonreflecting propagation of a spherical pressure wave generated by the laser-induced fragmentation of the nanoparticle from the CG water region into the infinite water environment. In the CG MD model, each particle represents several water molecules, and the degrees of freedom missing in such CG representation are accounted for through a heat bath approach that associates an internal energy variable with each CG particle. The energy exchange between the internal (implicit) and dynamic (explicit) degrees of freedom is controlled by the dynamic coupling between the translational degrees of freedom and the radial (breathing) mode associated with each CG particle.[41,71,72] The capacity of the internal heat bath associated with each CG particle, its mass, and the parameters of the interparticle interaction potential are chosen so that the experimental density and heat capacity of water are reproduced exactly, while other properties relevant to the simulation of laser ablation in water, such as the speed of sound, bulk modulus, viscosity, surface energy, melting temperature, critical temperature, and critical density, do not deviate from the experimental values for water by more than 25%.[41,71] The cross-interaction between Au atoms and the CG water particles is described by Lennard-Jones (LJ) potential with the length and energy parameters, σ = 2.63 Å and ε = 0.052 eV, fitted to the value of Au−water interfacial energy predicted in atomistic simulations,[118] 0.394 J/m^2.

The thickness of the CG water shell is 50 nm, which corresponds to around 11 million CG particles. This thickness is chosen to ensure that the products of the laser-induced fragmentation remain within the spherical computational domain with an initial radius of 60 nm simulated with the combination of atomistic and CG MD. The MD domain is enclosed by the acoustic impedance matching boundary condition based on an imaginary plane approach[75] adapted in this work for the spherical geometry of the problem. The

https://doi.org/10.1021/acs.jpcc.1c03146
J. Phys. Chem. C 2021, 125, 13413−13432

boundary condition takes the form of an imaginary infinitely thin spherical shell interacting with CG water particles through the Morse potential defined as a function of the distance between the surface of a CG particle and the shell. The imaginary shell moves (changes its radius) in response to forces acting on it from the CG water particles and an additional radial force $\vec{F}_e$ that mimics the elastic response of water located outside the spherical MD domain to forces acting from inside the MD domain. This additional force is proportional to the instantaneous radial velocity $\vec{v}_r$ of the imaginary shell and acts in the opposite direction, $\vec{F}_e = -Sz\vec{v}_r$, where S is the total surface area of the boundary shell and z is the far-field approximation of the acoustic impedance of water defined as $z = B\rho$, where B and ρ are the bulk modulus and density of the CG water.[41] The mass assigned to the imaginary plane is equal to the total mass of a monolayer of CG water particles, and the equation of motion is solved for the radius of the boundary shell together with the integration of the equations of motion for all the atoms and CG water particles.

3. RESULTS AND DISCUSSION

The new model described in the previous section is applied here for investigation of the mechanisms of LFL of a 20 nm Au nanoparticle irradiated by a 10 ps laser pulse at a laser fluence that supplies energy density that is ∼20% short of the energy needed for complete vaporization of the nanoparticle. The channels of the conversion and redistribution of energy deposited by the laser pulse are considered first in Section 3.1. The dynamics and mechanisms of LFL are discussed next, in Section 3.2, based on the visual picture of the fragmentation process and the evolution of temperature, pressure, and density in the irradiated system. The size distribution of the atomic clusters and nanoparticles is analyzed and connected to the fragmentation mechanisms and the nanobubble dynamics in Section 3.3. Finally, a detailed analysis of atomic trajectories leading to the formation of the atomic clusters and nanoparticles in LFL is provided and related to the crystallinity and shapes of the fragmentation products in Section 3.4.

3.1. Channels of the Energy Conversion. The analysis of the kinetics and channels of the conversion and redistribution of the deposited laser energy serves as the basic test of the newly developed model, provides a general picture of the interplay of different processes involved in LFL, and sets the stage for a more detailed discussion of the fragmentation mechanisms in the following sections. All energy components plotted in Figure 5 are normalized by the total energy deposited by the laser pulse and are calculated with respect to the reference levels in the initial 20 nm Au nanoparticle−water system equilibrated at 300 K. Thus, the normalized total energy of the system is zero before the laser irradiation, increases up to unity during the laser pulse, and is conserved for the rest of the simulation. The total energy conservation is an indicator of adequate technical performance of the combined TTM-MD model.[119]

Initially, during the 10 ps laser pulse, all the laser energy is deposited into the thermal energy of the electrons shown by the red dash-dotted line in Figure 5a. Since the laser pulse duration is comparable to the time of electron−phonon equilibration, the energy transfer from the excited electrons to the energy of atomic motions in the Au nanoparticle occurs simultaneously with the laser energy deposition. As a result, the maximum energy of the electrons reached at 30 ps (the time of the peak intensity of the Gaussian laser pulse) corresponds to only ∼40% of the total deposited energy. The energy transfer from the electrons to atomic motions continues after the laser pulse and completes by ∼200 ps. The consideration of the size dependence of electron−phonon coupling in metal nanoparticles and clusters described in Section 2.2 has a relatively small effect on the overall electron energy evolution predicted by the model.

The energy transfer from the excited electrons leads to the rapid heating of the Au nanoparticle, which in turn transfers the energy to the surrounding water. The energy transfer to the water environment proceeds through both the heat transfer and work done by the expanding nanoparticle. Both of these channels of the energy transfer are greatly enhanced by the explosive decomposition of the Au nanoparticle into vapor, atomic clusters, and small molten nanoparticles. As discussed below, in Section 3.2, the phase explosion of the nanoparticle generates a strong compressive wave in the water environment and leads to the rapid mixing and thermal equilibration of the products of the nanoparticle fragmentation with water. The energy carried away by the expanding spherical pressure wave from the computational system through the nonreflecting boundary is monitored and is shown in Figure 5a by the black dashed line. By the time of 1 ns, 78% of the energy deposited by the laser pulse is already converted into the (mostly thermal) energy of water, while an additional 12% of the energy is emitted in the form of the pressure wave.

The remaining 10% of the deposited energy at 1 ns is still associated with Au atoms. It is instructive to separate this energy into the thermal part related to the heating of Au above the initial temperature of 300 K and the nonthermal part associated with the energy of new surfaces produced by the fragmentation of the initial nanoparticle, as well as the energy of any internal structural defects present in the fragmentation products. An approximate separation of the Au energy into the two parts can be based on the virial theorem of the classical mechanics,[120] that is, assuming that the thermal energy of atomic motions includes equal contributions from the kinetic and potential energies. By subtracting the double kinetic energy from the total energy associated with Au atoms, the nonthermal potential energy is calculated and is shown by the dashed black line connecting the data points in Figure 5b. By the time of 1 ns, the nonthermal energy almost coincides with the total energy of the Au atoms, reflecting the fact that the products of the nanoparticle fragmentation are already thermally equilibrated with water at a temperature of ∼370 K by this time.

Interestingly, the nonthermal energy of Au decreases continuously starting from the maximum value of 28% at 80 ps. This decrease continues past the first nanosecond and brings the nonthermal energy of Au down to 6.7% by the time of 14.4 ns, close to the end of the simulation. This decrease is associated with the growth, agglomeration, and coalescence of Au clusters and nanoparticles, leading to the reduction of the total surface energy. The energy released in these processes goes mostly into the thermal energy of water, which increases up to 79.7%. The energy that goes into the pressure wave emission also increases to 13.6% by 14.4 ns, mostly due to the contribution from a wave associated with the collapse of a nanobubble generated in the course of the nanoparticle fragmentation (see next section). Overall, the "energy efficiency" of the laser-induced fragmentation, that is, the part of the energy that goes directly into the conversion of the initial nanoparticle into the fragmentation products, appears to

https://doi.org/10.1021/acs.jpcc.1c03146
J. Phys. Chem. C 2021, 125, 13413−13432

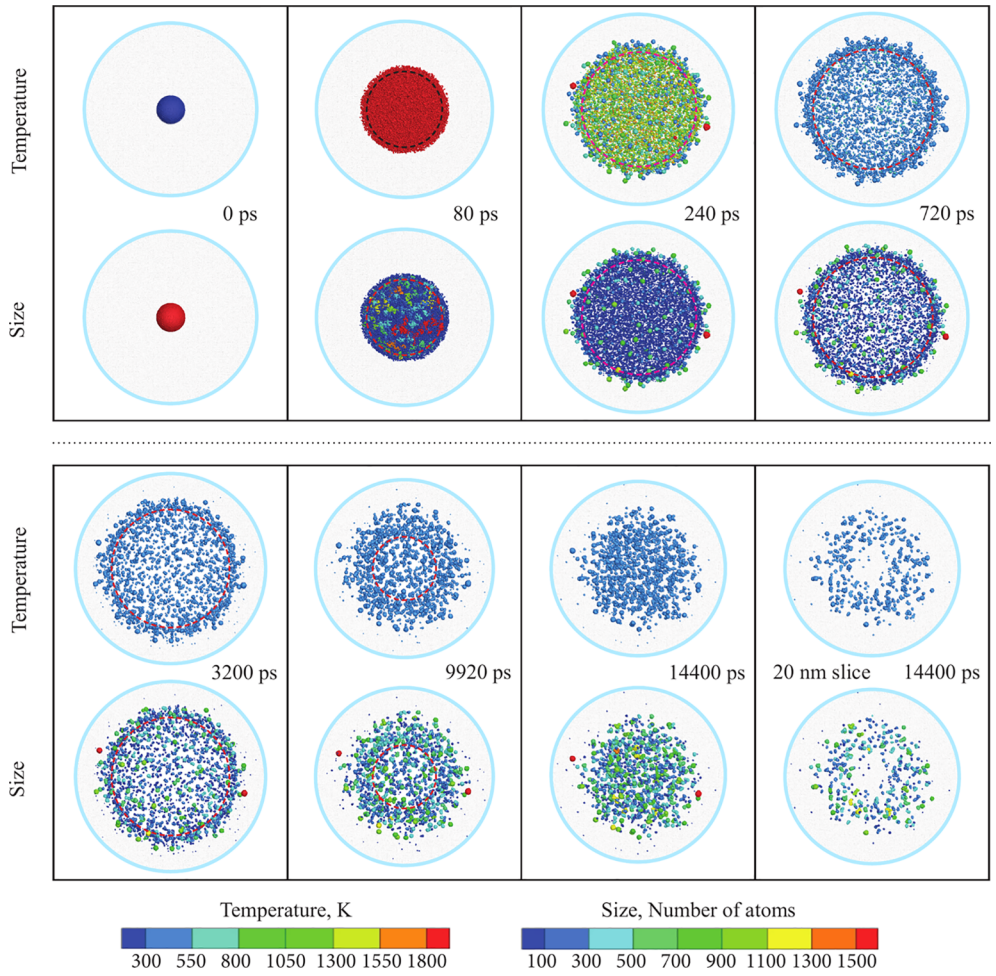

Figure 6. Snapshots from a simulation of LFL of a 20 nm Au nanoparticle irradiated by a 10 ps laser pulse at a laser fluence that results in the deposition of the total energy density of 3.6 eV/atom. The Au atoms are shown by dots colored according to the temperature (top rows) and the size of the clusters/nanoparticles they belong to (bottom rows). In the snapshots, all Au atoms are shown, except for the last panel, where only the Au atoms within a 20 nm-thick slice cut from the center of the system are shown for 14,400 ps. The CG water particles located within a 2 nm-thick slice cut from the central part of the system are shown by gray dots. The position of the boundary of the computational system is marked by a light-blue circle. The boundary of the nanobubble, defined as a location where the water density drops by 50% with respect to its initial value, is outlined by red or black dashed circles. An animated sequence of snapshots from this simulation with a time resolution of 80 ps is provided in the Supporting Information for this article.

be below 10% in the irradiation regime considered in the present study, with most of the energy going into the heating of water and generation of pressure waves.

3.2. Mechanisms of LFL and Nanobubble Dynamics.

The visual picture of the LFL process is provided in Figure 6, where a series of snapshots from the simulation of LFL is presented. Two representations of the same snapshots are shown in the top and bottom rows, where the Au atoms are colored by the temperature and size of the clusters/nanoparticles they belong to, respectively. The latter representation is enabled by the on-the-fly cluster analysis algorithm described in Section 2.3.

The first set of snapshots is shown for the initial system and is followed by the ones for a time of 80 ps after the start of the simulation (i.e., 55 ps after the 10 ps laser pulse reaches its peak intensity). By this time, most of the energy deposited by the laser pulse to the electronic subsystem is already transferred to the energy of atomic motions, bringing the atomic temperature to the levels that exceed the threshold for the phase explosion,[53−56] that is, an explosive decomposition of the superheated material into vapor, atomic clusters, and small liquid droplets. The products of the phase explosion push against the surrounding water, creating an expanding nanobubble that is initially almost completely free of water molecules. This emerging nanobubble is outlined by the dashed black and red circles in the top and bottom row snapshots shown for 80 ps, respectively.

Note that the large, branched cluster shown by red color in the lower row of snapshots at 80 ps does not correspond to any stable entity but is simply the result of the application of the cluster identification algorithm to an instantaneous atomic configuration of a dense hot mixture of vapor and atomic clusters undergoing rapid expansion. By the time of 240 ps, the expanding products of the phase explosion are already well separated into individual atoms, atomic clusters, and nanoparticles. It is interesting to note that, already at this early stage of the fragmentation process, a substantial fraction of the atoms (31%) already belongs to the nanoparticles with $D_e \geq$ 2.2 nm (more than 332 atoms). The major fraction of the fragmentation products emerging from the phase explosion of the nanoparticle is represented by atomic clusters with $D_e <$ 2.2

https://doi.org/10.1021/acs.jpcc.1c03146
J. Phys. Chem. C 2021, 125, 13413−13432

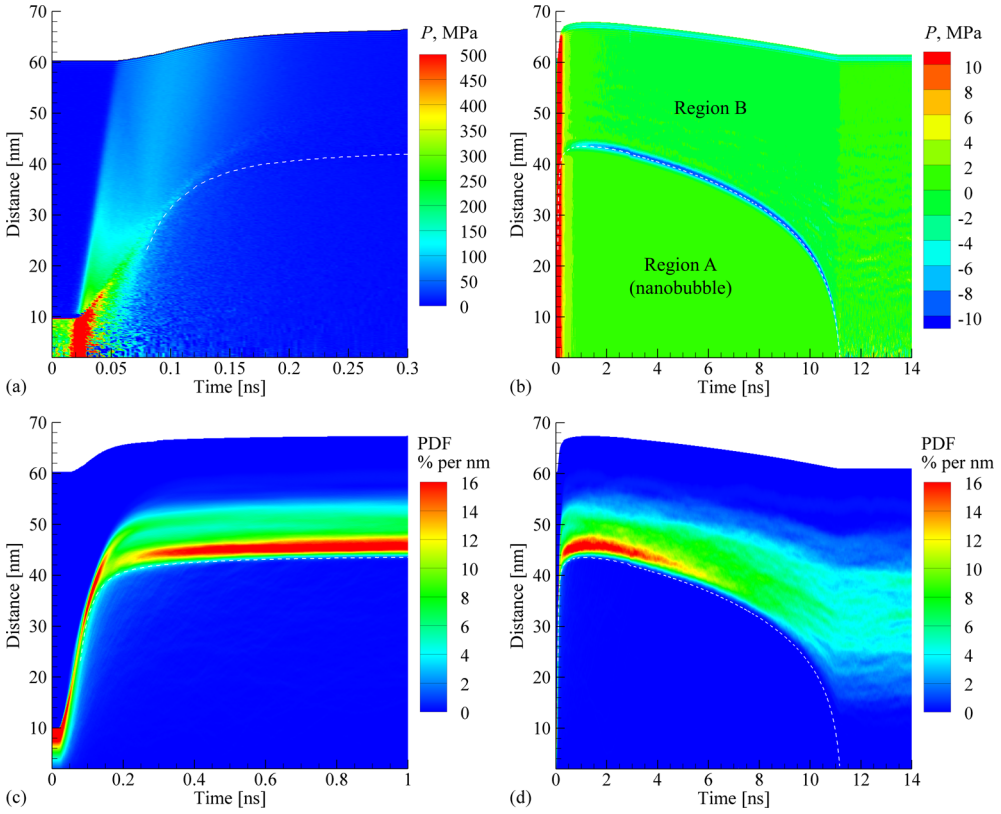

Figure 7. Spatial and temporal evolution of pressure (a, b) and probability density function characterizing the distribution of Au atoms (c, d) predicted in the simulation for which snapshots are shown in Figure 6. The contour plots are shown for the initial stage of the fragmentation process (300 ps for pressure and 1 ns for PDF) in the left panels (a,c) and for 14 ns in the right panels (b,d). The white dashed lines mark the boundary of the nanobubble, defined as a location where the water density drops by 50% with respect to its initial value. The evolution of average pressure in regions A and B marked in (b) is shown in Figure 8a.

nm (see Section 3.3 for detailed analysis of the cluster/nanoparticle generation mechanisms and size distribution).

The rapid transformation of the products of the explosive decomposition of the initial nanoparticle into atomic clusters and small nanoparticles proceeds simultaneously with cooling of the fragmentation products, as can be seen from the snapshots colored by the nanoparticle temperature. Only five particles have temperature exceeding 1800 K at 240 ps and are colored by red color in the corresponding snapshot in Figure 6. These are the two largest nanoparticles consisting of 1562 and 1941 atoms (red particles in the 240 ps snapshot colored by the nanoparticle size), as well as three smaller particles, one of which is located within the nanobubble and two others just transitioned from the nanobubble into the water environment. The rapid cooling of the metal clusters and nanoparticles can be attributed to the heat transfer to the surrounding water, as most of the fragmentation products are promptly injected beyond the edge of the expanding nanobubble, where the density of water is high (see the discussion of Figures 7c,d and 9 below).

By the time of 720 ps, even the largest nanoparticles almost completely equilibrate with the surrounding water, as evidenced by the uniform blue color of nanoparticles in the snapshot colored by temperature. The sizes of the nanoparticles, however, continue to evolve at a longer timescale, as can be seen from the increasing number of light green (D_e > 3.1 nm), yellow (D_e > 3.3 nm), orange (D_e > 3.5 nm), and red (D_e > 3.6 nm) nanoparticles in the snapshots colored by size in Figure 6. As discussed in more detail below, in Section 3.3, the coarsening of the nanoparticles mainly proceeds through agglomeration and coalescence, which are facilitated by the increase in the concentration of the colloidal solution of the fragmentation products due to the collapse of the nanobubble by 11.6 ns.

The generation and collapse of the nanobubble can be clearly seen from the contour plots of pressure and distribution of the fragmentation products (Au atoms, clusters, and nanoparticles) shown in Figure 7. The evolution of pressure at the initial stage of the nanobubble formation is shown in Figure 7a, where the color scale is chosen to highlight the large pressure, exceeding 500 MPa, generated by the explosive phase decomposition of the initial Au nanoparticle. This large pressure is responsible for the generation of a strong spherical pressure wave propagating toward the boundary of the system, where the nonreflecting boundary condition allows the wave to leave the computational domain with minimum reflection. The pressure generated by the phase explosion also drives the generation and rapid expansion of the nanobubble, as marked by the white dashed line in Figure 7a. Note that the region of elevated pressure transiently formed above the edge of the nanobubble is due to the implantation of the high-temperature products of the phase explosion into the water environment outside the expanding nanobubble.

The longer-term evolution of pressure is shown in Figure 7b in a color scale chosen to highlight the contribution of the surface tension at the boundary of the nanobubble, which shows up as a narrow strip of negative (blue) pressure. The initial rapid growth of the nanobubble during ~150 ps after the

https://doi.org/10.1021/acs.jpcc.1c03146
J. Phys. Chem. C 2021, 125, 13413−13432

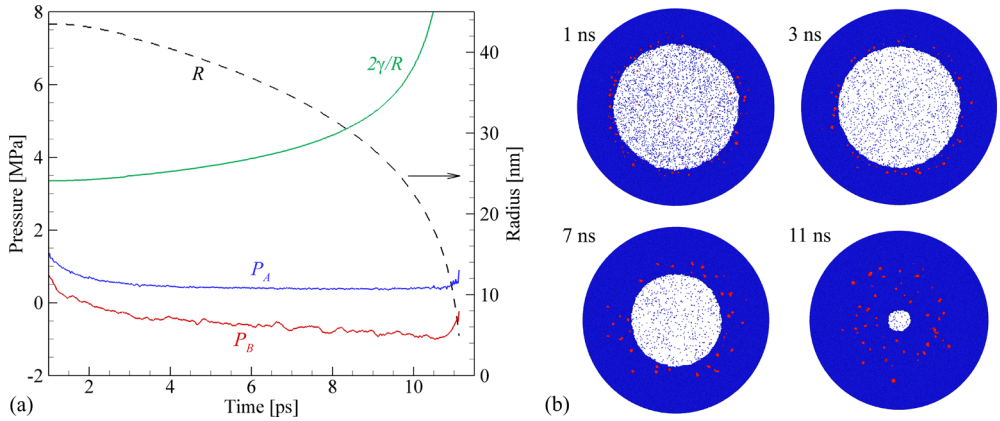

Figure 8. (a) Evolution of the radius of the nanobubble R, the corresponding Laplace pressure $2\gamma/R$, the pressure inside the nanobubble P_A (averaged over region A in Figure 7b), and pressure P_B outside the nanobubble (averaged over region B in Figure 7b). (b) Snapshots of 4 nm-thick slices cut from the middle of the simulation system and shown for 1, 3, 7, and 11 ns. The Au atoms and CG water particles in the snapshots are colored red and blue, respectively.

laser-induced phase explosion of the nanoparticle is followed by a much slower growth or stagnation during the following nanosecond. After reaching its maximum radius of ∼44 nm at ∼1 ns, the nanobubble starts to shrink with a rate increasing with time and finally collapses at 11.6 ns.

The conditions leading to the nanobubble collapse are illustrated in Figure 8a, where the average pressure inside and outside the nanobubble (regions A and B marked in Figure 7b) are plotted along with the Laplace pressure produced by the surface tension, $P_L = 2\gamma/R$, where γ is the surface energy of water and R is the radius of the bubble. Since the surface tension has been shown to exhibit a weak dependence on R for nanobubbles with radii down to a few nanometers,[121] the surface of the bubble consists almost exclusively of water (e.g., see snapshots in Figure 8b), and the temperature of water near the bubble at the time of the bubble collapse is close to the room temperature, the value of $\gamma = 0.073$ J/m^2 evaluated for the CG water at 300 K[41] (close to the experimental value for water, 0.072 J/m^2) is used in the analysis. As can be seen in Figure 8a, the disbalance between the Laplace pressure P_L and the pressure difference between the inside and outside of the nanobubble, $P_A - P_B$, increases with time and drives the rapidly accelerating nanobubble collapse. Interestingly, the internal pressure P_A remains almost constant for the most part of the nanobubble collapse. This can be explained by the relatively long timescale (∼10 ns) of the collapse, which allows the vapor density and pressure inside the nanobubble to stay close to the equilibrium values. The sharp increase in the vapor density and pressure is only observed during the last nanosecond of the nanobubble collapse.

The timescales of the expansion and collapse of the nanobubble predicted in the simulation can be related to the results of time-resolved optical and X-ray probing experiments. In the irradiation regime when nanoparticles melt but survive the irradiation, the relatively short nanobubble lifetimes of ∼400 ps for 9 nm nanoparticles[29] and 1.7 ns for 36 nm nanoparticles[30] irradiated by femtosecond pulses were evaluated based on pulsed X-ray scattering measurements. For larger 60 nm Au nanoparticles irradiated by 15 ps pulses, the nanobubble lifetime of around 10 ns was inferred from the results of optical pump−probe experiments.[28] A similar timescale of the nanobubble expansion and collapse was obtained in X-ray scattering measurements for 54 nm Au nanoparticles irradiated by ∼1 ps laser pulses in the laser fragmentation regime.[25] This timescale is in a good quantitative agreement with the 11.6 ns lifetime of the nanobubble predicted in the simulation. We note, however, that while the possibility of nanobubble rebound was suggested in ref 25, we do not observe any signs of the rebound following the nanobubble collapse in the simulation.

One striking observation apparent from the slices of the system shown in Figure 8b is the small number of Au clusters and nanoparticles inside the nanobubble at 1 ns and the nearly complete absence of Au inside the nanobubble at 3 ns and later. Indeed, only three clusters consisting of 32, 30, and 22 Au atoms are found inside the nanobubble after 3.3 ns, and only one 30-atom cluster is present after 4.3 ns (the other two clusters are absorbed by the bubble surface by this time). No Au atoms are present inside the bubble after 7.25 ns. The explosive phase decomposition of the irradiated nanoparticle is sufficiently vigorous to drive the prompt implantation/injection of the nanoparticle decomposition products into the dense liquid environment beyond the boundary of the rapidly expanding nanobubble. The rapid redistribution of gold from the 20 nm nanoparticle located in the center of the computational system to the region outside the boundary of the nanobubble is apparent from the contour plots, Figure 7c,d, showing the probability density function (PDF) characterizing the distribution of Au atoms. The PDF is defined so that the integral over distance from the center of the system calculated for any moment of time accounts for 100% of Au. An alternative representation of the redistribution of Au atoms in the course of the phase explosion is provided by the density profiles plotted in Figure 9.

It can be seen from Figures 7c and 9 that almost all of the Au clusters and nanoparticles that can be seen in the snapshots for 240 ps in Figure 6 are embedded into water and are located above the boundary of the nanobubble. During the nanobubble collapse, the Au clusters and nanoparticles are moving inward along with the water and are spreading out over a wider shell-shaped region extending from ∼10 to ∼50 nm from the center of the system, Figures 7d and 9. The volumetric mass density of Au, however, does not undergo a significant decrease during the nanobubble collapse, as can be seen from the density profiles shown for 3200, 9920, and 14,400 ps in Figure 9. The retention of the high concentration of Au clusters and

https://doi.org/10.1021/acs.jpcc.1c03146
J. Phys. Chem. C 2021, 125, 13413−13432

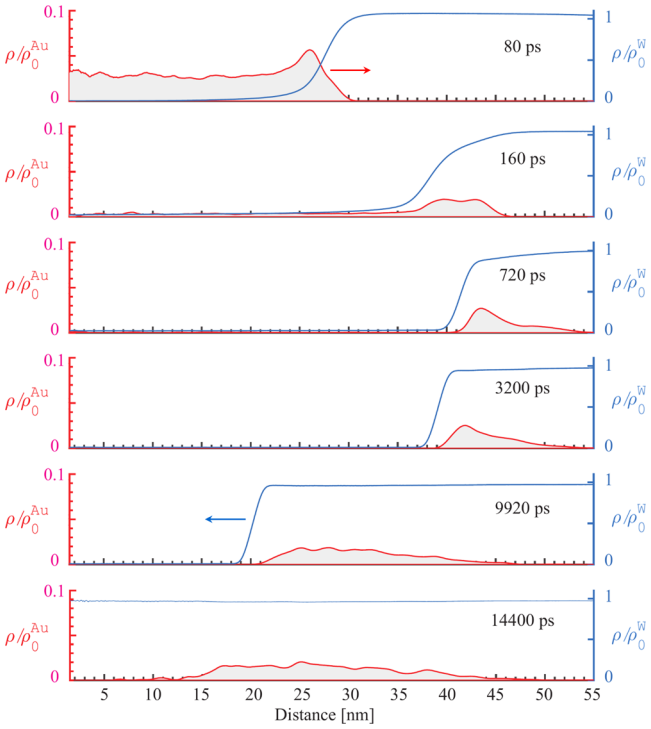

Figure 9. Water and Au density profiles plotted for different moments of time during the simulation illustrated by snapshots shown in Figure 6. The profiles are shown by blue lines for water and by red lines outlining gray areas for Au. The two arrows show the dominant processes driving the generation of the nanobubble (expansion of the products of the explosive decomposition of the nanoparticle, red arrow) and the collapse of the nanobubble (Laplace pressure produced by the surface tension, blue arrow). An animation showing the evolution of the density profiles is provided in the Supporting Information for this article.

nanoparticles after the nanobubble collapse creates the conditions amenable to the long-term nanoparticle growth and agglomeration beyond the timescale considered in the simulation. Interestingly, the central region of the system with a radius of ∼15 nm remains virtually free of nanoparticle fragmentation products, as can also be seen from the last panel of Figure 6, where a 20 nm-thick slice cut from the center of the system is shown for 14.4 ns.

3.3. Generation of Atomic Clusters and Nanoparticles. The computational predictions on the rapid implantation of the nanoparticle fragmentation products into the dense liquid environment and the high concentration of Au clusters and nanoparticles in a relatively narrow shell-like region surrounding the nanobubble, discussed in the previous section, have direct implications on the mechanisms and kinetics of the nanoparticle formation. At the initial stage of the LFL process, the irradiated nanoparticle undergoes an explosive decomposition into vapor, atomic clusters, and small liquid droplets. The products of the phase explosion push against the water environment and drive the formation and rapid expansion of a nanobubble, as can be seen from the density profiles for 80 ps in Figure 9. In contrast to earlier simulations of laser ablation in liquids,[41−43] where the interaction of the ablation plume with liquid environment leads to the formation of a transient hot metal layer at the plume−liquid interface, the relatively small amount of Au contained in the exploding nanoparticle and the rapid expansion of the surface area of the nanobubble leads to an effective mixing of the nanoparticle disintegration products with water. By the time of 160 ps, most of the Au particles are already "swallowed" by water and are located on the outer side of the emerging surface of the nanobubble; see Figure 7c and the density profiles for 160 ps in Figure 9.

When the Au atoms, clusters, and nanodroplets are incorporated into the dense water environment, they cool rapidly and form a highly supersaturated solution where the barrierless nucleation and growth of clusters and nanoparticles is only limited by the kinetics of diffusion in the water environment. The evolution of the mass-weighted distribution of effective diameters D_e of clusters and nanoparticles during the simulation is shown in Figure 10 in the form of PDF

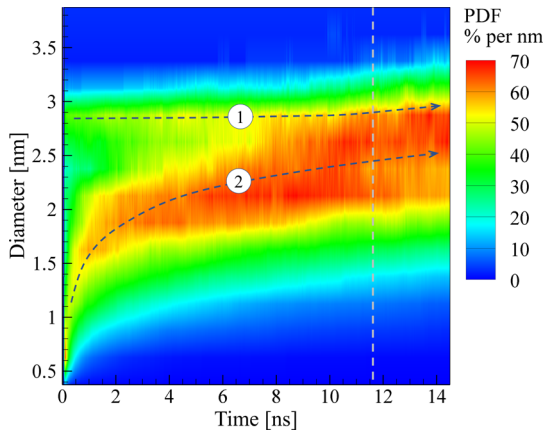

Figure 10. Evolution of the mass-weighted cluster/nanoparticle size distribution in a simulation of LFL illustrated in Figure 6. The distribution is shown in the form of the PDF calculated by dividing the total mass of clusters/nanoparticles that fall within size bins with a width of 0.25 nm by the bin width and by the total mass of Au in the system, and then multiplying by 100 to express PDF in units of % per nm. The two gray dashed arrows show two distinct channels of the nanoparticle formation. The vertical dashed line marks the time of the nanobubble collapse, 11.6 ns.

normalized so that, for any time, the integral over D_e would recover 100% of the mass of all the particles. The analysis of the distribution reveals two distinct pathways of the nanoparticle formation: (1) the direct/prompt formation of relatively large nanoparticles with diameters ranging from ∼2.5 to 3.96 nm (∼500−1941 atoms) and (2) nucleation and growth from atoms and atomic clusters gradually growing into nanoparticles with $D_e \geq 2.2$ nm.[82] These two pathways of the nanoparticle formation are schematically marked by dashed arrows in Figure 10. The first arrow shows a steady and slowly growing population of large nanoparticles generated during the first nanosecond after the laser pulse, while the second arrow follows the much more rapid growth of atomic clusters.

The coexistence of two distinct pathways of the nanoparticle formation is responsible for the early appearance of the bimodal mass-weighted particle size distribution that can be seen in Figure 11b. The distributions in Figure 11b correspond to five vertical cross sections of the contour plot shown in Figure 10. The distribution shown for 1 ns exhibits an apparent bimodal character, with most of the Au atoms contributing to the first broad peak that corresponds to atomic clusters with D_e < 2.2 nm (less than 333 atoms). As time progresses, however, this peak steadily shifts to larger sizes and eventually merges

https://doi.org/10.1021/acs.jpcc.1c03146
J. Phys. Chem. C 2021, 125, 13413−13432

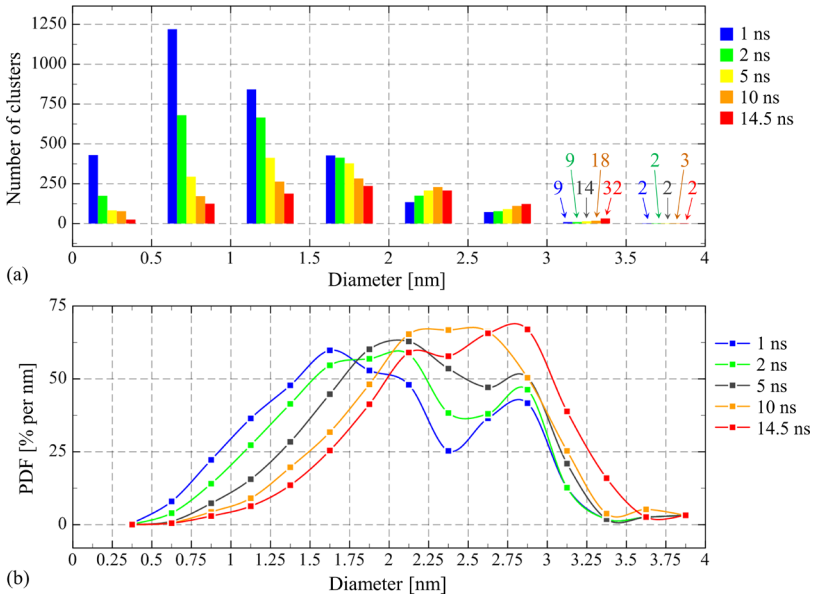

Figure 11. Evolution of the cluster/nanoparticle size distribution during the simulation of LFL illustrated in Figure 6, shown in the form of the number of clusters (a) and the PDF of the cluster mass distribution (b). Clusters are separated by diameter into bins with widths of 0.5 nm in (a) and 0.25 nm in (b). In (a), the numbers for clusters with diameters ranging from 3 to 3.5 nm and from 3.5 to 4 nm are listed in the panel. In (b), the values of the PDF for a given size bin is calculated by dividing the total mass of clusters that fall into the bin by the total mass of Au in the system and by the bin width, and then multiplying by 100 to express PDF in units of % per nm. No clusters larger than 4 nm are observed in the simulation. Individual atoms (monomers) are included in the counts for the first bins of the distributions.

with the second peak that corresponds to the nanoparticles. The total mass of the largest nanoparticles with D_e > 2.75 nm increases slowly over the first 10 ns but increases faster upon the nanobubble collapse, suggesting that the collapse stirs the colloidal solution and facilitates the agglomeration of nanoparticles.

The same process of the evolution of atomic clusters into nanoparticles on the nanosecond timescale can be seen from the number-weighted nanoparticle size distributions shown in Figure 11a. The number of atomic clusters with D_e < 2 nm steadily decreases with time, while the number of nanoparticles increases. Interestingly, the number of the largest nanoparticles with D_e > 3.5 stays at 2 until the end of the simulation (the third nanoparticle appearing in this range at 10 ns is the result of two nanoparticles composed of 801 and 796 atoms pathing within the interaction range from each other at 10 ns but not forming a stable joint nanoparticle). This observation highlights the distinction between the prompt generation of large nanoparticles (arrow ① in Figure 10) and the gradual growth of the nanoparticles by agglomeration of atomic clusters (arrow ② in Figure 10), as the second mechanism cannot increase the number of the largest nanoparticles on the timescale of the simulation.

The size distributions predicted in the simulation can be related to those obtained in the experimental study of LFL of 54 nm Au nanoparticles.[25] The mass-weighted size distributions obtained from analysis of the results of time-resolved low-angle X-ray scattering measurements are characterized by the dominant contribution from nanoparticles in the size range of 2−3 nm, with a noticeable presence of larger nanoparticles. This size range of fragmentation products, observed at the earliest delay of 30 ns, is in good agreement with the distribution predicted in the simulation for 14.5 ns, shortly after the nanobubble collapse, Figure 11b. Moreover, while the evolution of the nanoparticles on the microsecond timescale cannot be directly studied in the simulations, the gradual increase of the mean size of the nanoparticles from ∼2 nm at 30 ns to 3−4 nm at 10 μs is in agreement with the general trend observed in the simulation for the first 14.5 ns after the fragmentation. The experimental observation of the minor but noticeable presence of larger fragmentation products, in the range from around 7−25 nm, may be related to the distinct channel of the generation of large nanoparticles identified in the simulation and marked by the arrow ① in Figure 10. Given the much longer experimental timescales, however, the contribution of the nanoparticle agglomeration and coalescence to the population of the largest nanoparticles can also be significant.

The computational prediction of the massive generation of atomic clusters at the initial stage (first nanosecond) of LFL, followed by the rapid disappearance of the clusters due to the agglomeration and coalescence on the timescale of the nanobubble collapse (∼10 ns), has important practical implications. The atomic clusters exhibit highly attractive catalytic[97,122] and optical properties[93,95] that diminish as the size increases into the nanoparticle size domain. In particular, the Au clusters with D_e = 1.7 nm (144 atoms) have been found to display superior CO and ethanol oxidation activity with respect to smaller (nonmetallic) atomic clusters and larger (metallic) nanoparticles.[97] Similarly, small atomic Au islands on an inert substrate are found to serve as efficient catalysts for selective oxidation of styrene by dioxygen, while larger islands with diameters above ∼2 nm remain inactive.[122] The abundance of the atomic clusters in the transitional range of 1.2−2.2 nm at the initial stage of LFL (see the distribution for 1 ns in Figure 11b) and the observation that the clusters are already fully dissolved in the liquid environment outside the nanobubble at this early time, suggests an opportunity for preserving the population of the atomic clusters through the addition of surface-active solutes capable of suppressing the

https://doi.org/10.1021/acs.jpcc.1c03146
J. Phys. Chem. C 2021, 125, 13413−13432

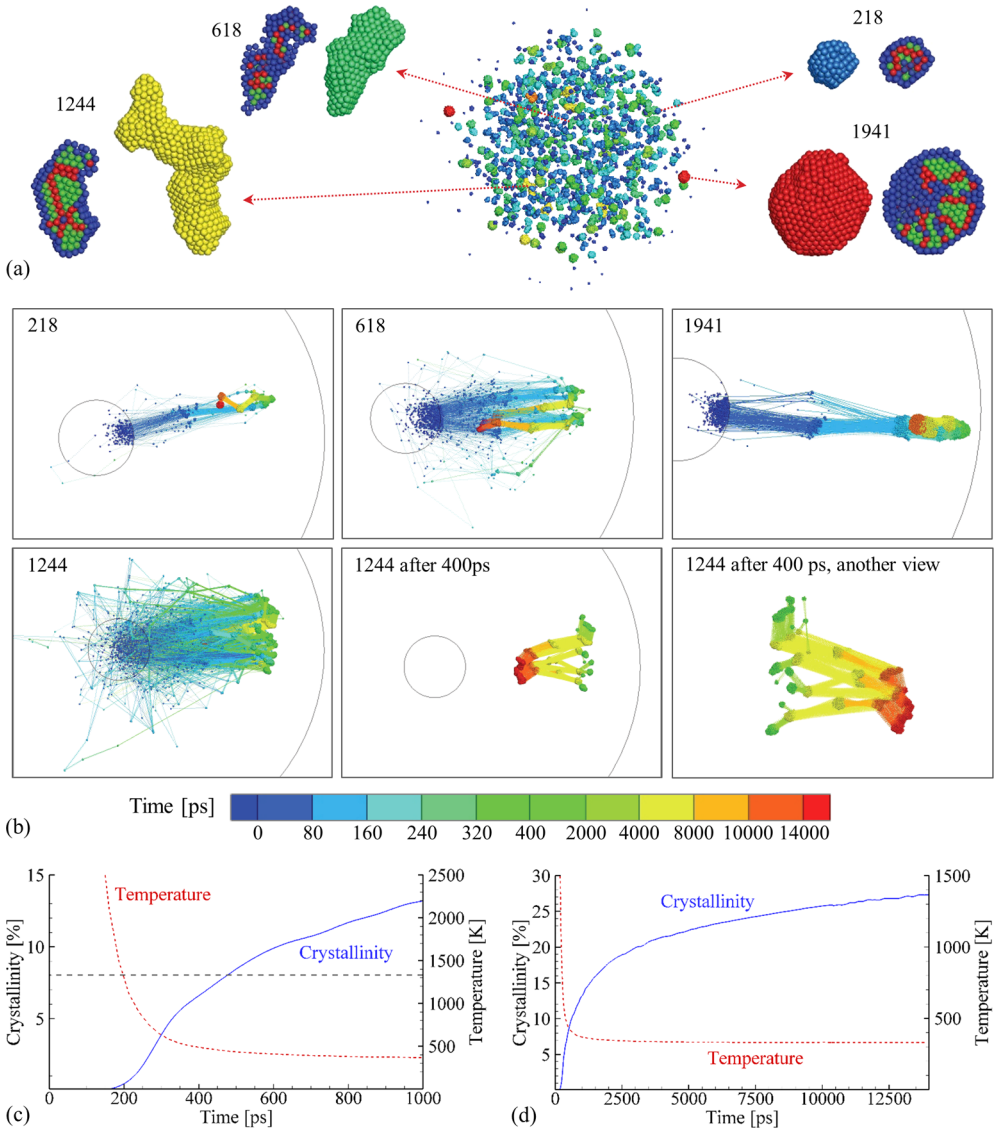

Figure 12. Atomistic view of the formation of nanoparticles and atomic clusters. (a) Whole configuration of the nanoparticle fragmentation products at 14.4 ns (central image) and enlarged views of four representative particles and their cross sections. In the central image, the clusters and nanoparticles are colored by their size, with the same color scale as in Figure 6. In the particle cross sections, the atoms are colored by the local structural environment so that the atoms with local fcc and hcp environment are colored green and red, respectively, while the surface atoms, grain boundaries, and other unidentified local atomic structures are colored blue. The four particles are labeled by the number of atoms they include. (b) Atomic trajectories of all atoms that end up in the four representative nanoparticles show in (a). The trajectories are colored by time and start at the location of the atoms in the initial 20 nm nanoparticle marked by a small circle. The segments of the larger circle show the outer boundary of the computational domain. For the nanoparticle consisting of 1244 atoms, two additional views of the trajectories starting from 400 ps are shown to further illustrate the nanoparticle formation mechanism. The view direction is the same as in the complete view in the first additional panel and is changed in the second one. (c,d) The temporal evolution of the average temperature and "crystallinity" of all products of the laser-induced fragmentation are shown for the first nanosecond in (c) and for the whole duration of the simulation in (d). The "crystallinity" is defined as a fraction of atoms with local fcc and hcp environment with respect to the total number of Au atoms. The equilibrium melting temperature of gold is marked by the horizontal dashed line in (c).

coalescence of the Au clusters in the solution.[123−127] Given the short time window existing for the size quenching of the atomic clusters (as can be seen from Figure 11b, most of the atomic clusters had already merged into nanoparticles by 14.5 ns), the selection of the surface-active agents and their concentration should be made through consideration of both the degree of cluster protection against the coalescence and the kinetics of the cluster stabilization. In particular, the results of an *in situ* probing of Au nanoparticle fragmentation kinetics in water and in an aqueous solution of NaCl and NaOH at 0.3 mM of each component suggests that the initial size evolution of the fragmentation products is largely unaffected by the presence of the electrolyte, although the electrolyte does limit the growth of the nanoparticles at a timescale of microseconds.[25]

3.4. Atomistic View of Nanoparticle Formation in LFL.

To provide mechanistic insights into the two channels of the nanoparticle formation marked as arrows ① and ② in Figure 10, in this section, we report the results of a detailed analysis of atomic trajectories contributing to the formation of four representative nanoparticles. The locations of these nanoparticles at the end of the simulation and enlarged views of the

https://doi.org/10.1021/acs.jpcc.1c03146
J. Phys. Chem. C 2021, 125, 13413−13432

nanoparticles are shown in Figure 12a. The nanoparticles are labeled by the number of atoms they consist of at the end of the simulation. The nanoparticles with 618 and 1244 atoms end up in the central part of the cloud of the fragmentation products and feature irregular nonspherical shapes. In contrast, the cluster of 218 atoms and nanoparticle consisting of 1941 atoms are located at the periphery of the final distribution of the fragmentation products and have close-to-spherical shapes.

The shapes of the fragments can be correlated not just with their final location in the cloud of the fragmentation products but, more generally, with the particle formation mechanism illustrated in Figure 12b. This figure shows the atomic trajectories of all atoms that end up in the four representative particles by the end of the simulation. The trajectories are colored by time and originate from the location of the atoms within the initial nanoparticle before the irradiation outlined by a small circle. The atoms contributing to the two nanoparticles characterized by irregular shapes (618-atom and 1244-atom ones) tend to originate from the interior of the initial nanoparticle and are widely scattered at the initial stage of the fragmentation process. Within several hundreds of picoseconds, the atoms condense into many small clusters that are reflected from the expanding front of the emerging nanobubble and agglomerate into the final nanoparticles on the timescale of nanoseconds. This nanoparticle formation mechanism can be associated with the kinetic pathway of the nanoparticle formation marked by arrow ② in Figure 10.

The formation of the other two particles illustrated in Figure 12b, the 218-atom cluster and the largest nanoparticle consisting of 1941 atoms (D_e = 3.96 nm), has a different character. Most of the atoms contributing to these particles originate from the surface region of the initial nanoparticle. These atoms are vigorously propelled by the explosive phase decomposition of the interior part of the nanoparticle and penetrate deep into the water environment. Most of the atoms contributing to these particles stay together from the start of the fragmentation process and, by the time of 160 ps (light-blue points in the trajectories shown in Figure 12b), most of the atoms present in the final 218-atom cluster and all of the atoms present in the 1941-atom nanoparticle are already arranged into corresponding single particles. The prompt generation of the largest 1941-atom nanoparticle within just 130 ps after the laser pulse (counting from the peak power of the pulse at 30 ps to the time of 160 ps, for which the third set of points is plotted along the atomic trajectories) is particularly notable and provides a clear example of the nanoparticle formation pathway shown by arrow ① in Figure 10.

The apparent difference between shapes of the nanoparticles formed through the two different mechanisms discussed above is largely defined by the rapid quenching and crystallization of Au clusters and droplets injected into the water environment by the explosive phase decomposition of the irradiated nanoparticle. As can be seen in Figure 12c, the temperature averaged over all the nanoparticle fragmentation products drops below the equilibrium melting temperature of Au at ∼200 ps and continues to decrease down to ∼330 K at the end of the simulation. The cooling rate has some dependence on the Au particle size but is still extremely high for all nanoparticle fragments. For example, the temperature drops below the melting temperature by ∼160 ps for 218-atom cluster illustrated in Figure 12a,b and by ∼310 ps for the largest 1941-atom nanoparticle. The very efficient heat transfer from hot Au clusters and nanoparticles to the surrounding water can be attributed to the high curvature of the particle−liquid interface,[33,34] which prevents the formation of an insulating vapor layer and sustains the high interfacial heat flux even when the temperature of the Au particle exceeds the critical temperature of the surrounding liquid.

The rapid cooling of the fragmentation products triggers crystallization, which starts from the smaller clusters and nanoparticles at ∼200 ps and ends with complete solidification of the largest nanoparticles by ∼800 ps. The kinetics of crystallization is quantified in Figure 12c by "crystallinity" defined as a fraction of atoms with local face-centered cubic (fcc) and hexagonal close-packed (hcp) environments. We note, however, that "crystallinity" only accounts for the crystalline atoms in the interior of the nanoparticles and atomic clusters and excludes the surface atoms even for nanoparticles with a perfect crystalline structure. The long-term increase of the "crystallinity" after 700 ps is mainly related to the agglomeration of the crystalline nanoparticles, leading to the decrease in the number of surface atoms.

Since the particles generated along the pathway shown by arrow ① in Figure 10 are injected into the water environment as compact liquid droplets, the crystallization of these particles produces shapes close to spherical ones, for example, 218-atom and 1941-atom particles in Figure 12a. In contrast, the pathway shown by arrow ② in Figure 10 corresponds to the particles formed more gradually, on the nanosecond timescale, through agglomeration of atomic clusters and small nanoparticles that are already solidified at a time when they join together. Such process yields nanoparticles featuring irregular shapes and internal grain boundaries, as exemplified by 618-atom and 1244-atom particles in Figure 12a.

To further illustrate the process of nanoparticle agglomeration, two additional views of the atomic trajectories are shown in Figure 12b for the 1244-atom particle, where the initial 400 ps part of the trajectories is blanked. One can see that the final nanoparticle is formed through a gradual agglomeration of around a dozen smaller nanoparticles and clusters existing at 400 ps. By the time of 10 ns, there are two irregularly shaped solid nanoparticles separated from each other. The two nanoparticles join together at the final stage of the nanobubble collapse and form an elongated spiral structure that can be seen in Figure 12a. The observation that the final step of the nanoparticle growth coincides with the nanobubble collapse supports the notion of the contribution of the nanobubble collapse to the nanoparticle agglomeration discussed above, in Section 3.3, based on the increase in the mass fraction of the largest nanoparticles at the time of the nanobubble collapse observed in Figure 11b.

The rapid crystallization of the fragmentation products occurring within the outer layer of the nanobubble, prior to the nanobubble collapse, is an intriguing computational prediction that still awaits experimental confirmation. Indeed, the reappearance of powder diffraction peaks related to the presence of crystalline particles has only been observed at the end of the nanobubble collapse at around 10 ns in a recent time-resolved X-ray probing of the dynamics of picosecond LFL of Au nanoparticles.[25] We note that the characteristic size of the crystalline domains estimated from the peak broadening using the Scherrer equation is around 2 nm in the experimental study. This characteristic size is still larger than the size of the crystalline domains present in the largest fully crystallized nanoparticles, even if the size of the nanoparticle itself is larger than 2 nm. For example, the cross section of the largest

https://doi.org/10.1021/acs.jpcc.1c03146
J. Phys. Chem. C 2021, 125, 13413−13432

nanoparticle with a diameter of 3.96 nm shown in Figure 12a reveals the presence of twin boundaries (red planes in the cross section colored by local crystal structure) splitting the nanoparticle into nanometer-size fcc domains that could be too small to be resolved in the experimental probing. The highly defected nanotwinned structure of the nanoparticles can be attributed to the ultrafast quenching rate experienced by the fragmentation products and similar to that observed in earlier simulations of nanoparticle generation by laser ablation in liquid environment.[41−43] In addition to the high density of internal crystal defects, the presence of the nanobubble itself can further complicate the interpretation of the results of X-ray diffraction probing of the nanoparticle crystallinity at the early stage of the fragmentation process.

The excess energy associated with the high density of crystal defects in the nanoparticles may drive the internal structural relaxation and growth of defect-free crystalline domains within the nanoparticles. Moreover, the continuation of growth of the nanoparticles through agglomeration and coalescence illustrated by Figures 11b and 12d beyond the timescale of the simulation, as well as the slow shape relaxation driven by surface energy minimization,[128] may all contribute to the experimentally observed gradual recovery of the crystalline diffraction peaks on the timescale of hundreds of nanoseconds.[25]

Note that under typical LFL conditions, the products of nanoparticle fragmentation are often exposed to repetitive irradiation by additional laser pulses, which may strongly affect the final size and shape distributions of the nanoparticles generated by LFL. In particular, the scarcity of observations of irregularly shaped elongated nanoparticles,[129,130] such as the ones shown on the left side of Figure 12a, may be related to the enhanced broadband plasmon absorption by such nanoparticles,[130−132] leading to their preferential remelting and resolidification into spherical shapes. Moreover, the processes of nanoparticle agglomeration and coalescence are sensitive to the properties of the liquid medium, cautioning against overgeneralization of the long-term evolution of the nanoparticles observed in the simulations.

4. SUMMARY

A computational model suitable for investigation of laser-induced fragmentation of metal nanoparticles in a liquid environment is developed and parametrized for Au nanoparticles in water. The model combines a fully atomistic TTM-MD description of laser interaction with a metal nanoparticle, a CG representation of liquid environment, and an acoustic impedance matching boundary condition allowing the non-reflecting transmission of laser-induced spherical pressure wave through the boundary of the computational domain. A key feature of the model is the on-the-fly identification of all atomic clusters and nanoparticles in the course of the simulation, which enables a realistic description of the size dependence of the electron−phonon coupling strength and a precise analysis of the mechanisms and channels of the generation of nanoparticles and atomic clusters in LFLs. While the current version of the model does not account for the electrostatic fragmentation channel, the ability of the model to predict the electron temperature evolution makes it possible to include a description of the electron emission as well as electrostatic contribution to the nanoparticle fragmentation and stabilization of the fragmentation products in the future.

As the first application of the newly developed model, we investigate the dynamics and atomic-scale mechanisms of laser fragmentation of a 20 nm Au nanoparticle irradiated in water by a 10 ps laser pulse that supplies energy density comparable to that needed for complete vaporization of the nanoparticle. The irradiated nanoparticle is observed to undergo an explosive decomposition into vapor, atomic clusters, and small liquid droplets. The products of the phase explosion push against the surrounding water, creating a rapidly expanding nanobubble with the radius exceeding 40 nm by 200 ps after the laser pulse. The fragmentation products are promptly injected into the water beyond the edge of the expanding nanobubble and cool down due to the interaction with the cold water environment. The rapid growth of the nanobubble is followed by a much slower deflation driven by the Laplace pressure produced by the surface tension, leading to the collapse of the nanobubble at 11.6 ns. The lifetime of the nanobubble observed in the simulation is consistent with the results of time-resolved optical and X-ray probing of nanobubbles generated around the irradiated nanoparticles in the laser fragmentation regime.

The analysis of redistribution of energy deposited by the laser pulse has revealed the dominant channels of the energy conversion. While all the laser energy is initially deposited into the electronic excitation, the electron−phonon coupling leads to a rapid (on the timescale of tens of picoseconds) energy transfer from the electrons to the atomic motions in the Au nanoparticle. The rapid heating of the Au nanoparticle leads to the explosive decomposition of the nanoparticle into vapor, atomic clusters, and small molten nanodroplets, which in turn greatly accelerates the energy transfer to the surrounding water. For the most part, the energy transformation to the thermal energy of water and the energy of an outgoing spherical pressure wave generated in the water environment occurs within the first ∼200 ps after the laser pulse. Overall, the "energy efficiency" of the laser fragmentation, defined as the fraction of the deposited laser energy that goes into the formation of new surfaces upon the nanoparticle fragmentation, is found to be below 10%, with most of the deposited energy going into the heating of water (∼80%) and the emission of the pressure waves (more than 10%).

The detailed analysis of the nanoparticle fragmentation mechanisms reveals two distinct pathways of the formation of the fragmentation products: (1) the direct and prompt (within ∼100−200 ps) generation of relatively large nanoparticles with diameters ranging from ∼2.5 to 4 nm and (2) the much more gradual growth of smaller nanoparticles proceeding through agglomeration and coalescence of atomic clusters on the timescale of tens of nanoseconds. The coexistence of the two pathways of the nanoparticle formation is responsible for the early appearance of a bimodal mass-weighted particle size distribution featuring a broad peak that corresponds to atomic clusters with D_e < 2.2 nm (less than 333 atoms) and a narrower peak corresponding to larger nanoparticles with diameters up to 4 nm. As time progresses, the agglomeration and coalescence of atomic clusters shift the peak that corresponds to the clusters to larger sizes, leading to the formation of an almost unimodal nanoparticle size distribution by the time of the nanobubble collapse at 11.6 ns. The relatively narrow mass-weighted size distribution featuring a peak in the range of 2−3 nm, emerging by the end of the simulation at 14.5 ns, shortly after the nanobubble collapse, is in a good agreement with experimental distributions derived

https://doi.org/10.1021/acs.jpcc.1c03146
J. Phys. Chem. C 2021, 125, 13413−13432

from time-resolved X-ray scattering measurements and *ex situ* characterization of fragments generated by LFL of Au nanoparticles under comparable irradiation conditions.

The rapid injection of all the products of the nanoparticle fragmentation into the dense liquid environment at the early stage of the nanoparticle fragmentation has a strong impact not only on the long-term evolution of the size distribution of the atomic clusters and nanoparticles but also on their shapes and crystallinity. All of the clusters and nanoparticles are rapidly quenched by the surrounding water and crystallize during a short time span between 200 and 800 ps after the laser pulse. The crystallization of the nanoparticles produced through the direct injection of droplets deep into the water environment yields nanoparticles with close-to-spherical shapes, while the nanoparticles formed through a gradual agglomeration of already solidified atomic clusters and small nanoparticles have irregular elongated shapes. All nanoparticles feature a high density of twin boundaries and other crystal defects generated by the ultrafast quenching of the particles by the water environment and through the growth by agglomeration of smaller particles.

The computational predictions of the prompt generation of a high concentration of Au clusters and nanoparticles in a relatively narrow shell-like region on the outer side of the nanobubble and the rapid solidification of the fragmentation products at the early stage of the nanobubble formation have important practical implications for the design of new methods aimed at achieving an improved control over the size, shape, and composition of nanoparticles produced by LFL. The fast rate and the small scale of the laser-induced structural and phase transformations predicted in the first atomistic simulation of LFL also present a new challenge for the time-resolved X-ray or electron diffraction probing of the active processes occurring just outside the laser-generated nanobubble.

■ ASSOCIATED CONTENT

Supporting Information

The Supporting Information is available free of charge at https://pubs.acs.org/doi/10.1021/acs.jpcc.1c03146.

Animated sequences of snapshots and evolution of density profiles from the simulation of LFL (ZIP)

■ AUTHOR INFORMATION

Corresponding Author

Leonid V. Zhigilei − *Department of Materials Science and Engineering, University of Virginia, Charlottesville, Virginia 22904-4745, United States;* orcid.org/0000-0002-1549-7086; Email: lz2n@virginia.edu

Author

Hao Huang − *Department of Materials Science and Engineering, University of Virginia, Charlottesville, Virginia 22904-4745, United States*

Complete contact information is available at: https://pubs.acs.org/10.1021/acs.jpcc.1c03146

Author Contributions

H.H. and L.V.Z. contributed to the design and implementation of the computational model, to the analysis of the results, and to the writing of the manuscript.

Notes

The authors declare no competing financial interest.

■ ACKNOWLEDGMENTS

Financial support for this work was provided by the National Science Foundation (NSF) through grants CMMI-1663429 and DMR-1610936. Computational support was provided by the NSF through the Extreme Science and Engineering Discovery Environment (project TG-DMR110090). L.V.Z. also acknowledges the Mercator Fellowship at the University of Duisburg-Essen, Germany, funded by Deutsche Forschungsgemeinschaft (BA 3580/22-1). The authors thank Cheng-Yu Shih, Maxim Shugaev, Chaobo Chen, and Mikhail Arefev (University of Virginia) for useful suggestions on the technical aspects of the model, as well as Anna Ziefuss, Sven Reichenberger, Stephan Barcikowski (University of Duisburg-Essen), and Anton Plech (Karlsruhe Institute of Technology) for insightful discussion of the mechanisms of laser fragmentation in liquids.

■ REFERENCES

(1) Sztandera, K.; Gorzkiewicz, M.; Klajnert-Maculewicz, B. Gold nanoparticles in cancer treatment. *Mol. Pharm.* **2018**, *16*, 1−23.

(2) Pitsillides, C. M.; Joe, E. K.; Wei, X.; Anderson, R. R.; Lin, C. P. Selective cell targeting with light-absorbing microparticles and nanoparticles. *Biophys. J.* **2003**, *84*, 4023−4032.

(3) Lapotko, D.; Lukianova, E.; Potapnev, M.; Aleinikova, O.; Oraevsky, A. Method of laser activated nano-thermolysis for elimination of tumor cells. *Canc. Lett.* **2006**, *239*, 36−45.

(4) Jain, P. K.; Lee, K. S.; El-Sayed, I. H.; El-Sayed, M. A. Calculated absorption and scattering properties of gold nanoparticles of different size, shape, and composition: Applications in biological imaging and biomedicine. *J. Phys. Chem. B* **2006**, *110*, 7238−7248.

(5) Lemaster, J. E.; Jokerst, J. V. What is new in nanoparticle-based photoacoustic imaging? *Wiley Interdiscip. Rev.: Nanomed. Nanobiotechnol.* **2017**, *9*, No. e1404.

(6) Krawinkel, J.; Richter, U.; Torres-Mapa, M. L.; Westermann, M.; Gamrad, L.; Rehbock, C.; Barcikowski, S.; Heisterkamp, A. Optical and electron microscopy study of laser-based intracellular molecule delivery using peptide-conjugated photodispersible gold nanoparticle agglomerates. *J. Nanobiotechnol.* **2016**, *14*, 2.

(7) Zhang, Z.; Taylor, M.; Collins, C.; Haworth, S.; Shi, Z.; Yuan, Z.; He, X.; Cao, Z.; Park, Y. C. Light-activatable theranostic agents for image-monitored controlled drug delivery. *ACS Appl. Mater. Interfaces* **2018**, *10*, 1534−1543.

(8) Zhang, D.; Gökce, B.; Barcikowski, S. Laser synthesis and processing of colloids: Fundamentals and applications. *Chem. Rev.* **2017**, *117*, 3990−4103.

(9) Kanitz, A.; Kalus, M.-R.; Gurevich, E. L.; Ostendorf, A.; Barcikowski, S.; Amans, D. Review on experimental and theoretical investigations of the early stage, femtoseconds to microseconds processes during laser ablation in liquid-phase for the synthesis of colloidal nanoparticles. *Plasma Sources Sci. Technol.* **2019**, *28*, 103001.

(10) Barcikowski, S.; Plech, A.; Suslick, K. S.; Vogel, A. Materials synthesis in a bubble. *MRS Bull.* **2019**, *44*, 382−391.

(11) Wang, H.; Pyatenko, A.; Kawaguchi, K.; Li, X.; Swiatkowska-Warkocka, Z.; Koshizaki, N. Selective pulsed heating for the synthesis of semiconductor and metal submicrometer spheres. *Angew. Chem., Int. Ed.* **2010**, *49*, 6361−6364.

(12) Tsuji, T.; Yahata, T.; Yasutomo, M.; Igawa, K.; Tsuji, M.; Ishikawa, Y.; Koshizaki, N. Preparation and investigation of the formation mechanism of submicron-sized spherical particles of gold using laser ablation and laser irradiation in liquids. *Phys. Chem. Chem. Phys.* **2013**, *15*, 3099−3107.

(13) Link, S.; Burda, C.; Nikoobakht, B.; El-Sayed, M. A. Laser-induced shape changes of colloidal gold nanorods using femtosecond and nanosecond laser pulses. *J. Phys. Chem. B* **2000**, *104*, 6152−6163.

(14) Plech, A.; Ibrahimkutty, S.; Reich, S.; Newby, G. Thermal dynamics of pulsed-laser excited gold nanorods in suspension. *Nanoscale* **2017**, *9*, 17284−17292.
(15) Fazio, E.; Saija, R.; Santoro, M.; Abir, S.; Neri, F.; Tommasini, M.; Ossi, P. M. On the optical properties of Ag-Au colloidal alloys pulsed laser ablated in liquid: Experiments and theory. *J. Phys. Chem. C* **2020**, *124*, 24930−24939.
(16) Takami, A.; Kurita, H.; Koda, S. Laser-induced size reduction of noble metal particles. *J. Phys. Chem. B* **1999**, *103*, 1226−1232.
(17) Mafuné, F.; Kohno, J.-y.; Takeda, Y.; Kondow, T. Growth of gold clusters into nanoparticles in a solution following laser-induced fragmentation. *J. Phys. Chem. B* **2002**, *106*, 8555−8561.
(18) Inasawa, S.; Sugiyama, M.; Yamaguchi, Y. Bimodal size distribution of gold nanoparticles under picosecond laser pulses. *J. Phys. Chem. B* **2005**, *109*, 9404−9410.
(19) Amendola, V.; Meneghetti, M. Controlled size manipulation of free gold nanoparticles by laser irradiation and their facile bioconjugation. *J. Mater. Chem.* **2007**, *17*, 4705−4710.
(20) Giammanco, F.; Giorgetti, E.; Marsili, P.; Giusti, A. Experimental and theoretical analysis of photofragmentation of Au nanoparticles by picosecond laser radiation. *J. Phys. Chem. C* **2010**, *114*, 3354−3363.
(21) Werner, D.; Furube, A.; Okamoto, T.; Hashimoto, S. Femtosecond laser-induced size reduction of aqueous gold nanoparticles: In situ and pump−probe spectroscopy investigations revealing Coulomb explosion. *J. Phys. Chem. C* **2011**, *115*, 8503−8512.
(22) Hashimoto, S.; Werner, D.; Uwada, T. Studies on the interaction of pulsed lasers with plasmonic gold nanoparticles toward light manipulation, heat management, and nanofabrication. *J. Photochem. Photobiol., C* **2012**, *13*, 28−54.
(23) Werner, D.; Hashimoto, S. Controlling the pulsed-laser-induced size reduction of Au and Ag nanoparticles via changes in the external pressure, laser intensity, and excitation wavelength. *Langmuir* **2013**, *29*, 1295−1302.
(24) Ziefuß, A. R.; Reichenberger, S.; Rehbock, C.; Chakraborty, I.; Gharib, M.; Parak, W. J.; Barcikowski, S. Laser fragmentation of colloidal gold nanoparticles with high-intensity nanosecond pulses is driven by a single-step fragmentation mechanism with a defined educt particle-size threshold. *J. Phys. Chem. C* **2018**, *122*, 22125.
(25) Ziefuss, A. R.; Reich, S.; Reichenberger, S.; Levantino, M.; Plech, A. In situ structural kinetics of picosecond laser-induced heating and fragmentation of colloidal gold spheres. *Phys. Chem. Chem. Phys.* **2020**, *22*, 4993−5001.
(26) Hu, M.; Hartland, G. V. Heat dissipation for Au particles in aqueous solution: Relaxation time versus size. *J. Phys. Chem. B* **2002**, *106*, 7029−7033.
(27) Lapotko, D. Optical excitation and detection of vapor bubbles around plasmonic nanoparticles. *Opt. Express* **2009**, *17*, 2538−2556.
(28) Katayama, T.; Setoura, K.; Werner, D.; Miyasaka, H.; Hashimoto, S. Picosecond-to-nanosecond dynamics of plasmonic nanobubbles from pump-probe spectral measurements of aqueous colloidal gold nanoparticles. *Langmuir* **2014**, *30*, 9504−9513.
(29) Kotaidis, V.; Plech, A. Cavitation dynamics on the nanoscale. *Appl. Phys. Lett.* **2005**, *87*, 213102.
(30) Siems, A.; Weber, S. A. L.; Boneberg, J.; Plech, A. Thermodynamics of nanosecond nanobubble formation at laser-excited metal nanoparticles. *New J. Phys.* **2011**, *13*, 043018.
(31) Metwally, K.; Mensah, S.; Baffou, G. Fluence threshold for photothermal bubble generation using plasmonic nanoparticles. *J. Phys. Chem. C* **2015**, *119*, 28586−28596.
(32) Baffou, G.; Rigneault, H. Femtosecond-pulsed optical heating of gold nanoparticles. *Phys. Rev. B: Condens. Matter Mater. Phys.* **2011**, *84*, 035415.
(33) Merabia, S.; Keblinski, P.; Joly, L.; Lewis, L. J.; Barrat, J.-L. Critical heat flux around strongly heated nanoparticles. *Phys. Rev. E: Stat., Nonlinear, Soft Matter Phys.* **2009**, *79*, 021404.
(34) Merabia, S.; Shenogin, S.; Joly, L.; Keblinski, P.; Barrat, J.-L. Heat transfer from nanoparticles: A corresponding state analysis. *Proc. Natl. Acad. Sci. U.S.A.* **2009**, *106*, 15113−15118.
(35) Dou, Y.; Zhigilei, L. V.; Winograd, N.; Garrison, B. J. Explosive boiling of water films adjacent to heated surfaces: A microscopic description. *J. Phys. Chem. A* **2001**, *105*, 2748−2755.
(36) Sasikumar, K.; Keblinski, P. Molecular dynamics investigation of nanoscale cavitation dynamics. *J. Chem. Phys.* **2014**, *141*, 234508.
(37) Volkov, A. N.; Sevilla, C.; Zhigilei, L. V. Numerical modeling of short pulse laser interaction with Au nanoparticle surrounded by water. *Appl. Surf. Sci.* **2007**, *253*, 6394−6399.
(38) Lombard, J.; Biben, T.; Merabia, S. Threshold for vapor nanobubble generation around plasmonic nanoparticles. *J. Phys. Chem. C* **2017**, *121*, 15402−15415.
(39) Lombard, J.; Biben, T.; Merabia, S. Ballistic heat transport in laser generated nano-bubbles. *Nanoscale* **2016**, *8*, 14870−14876.
(40) Hu, M.; Poulikakos, D.; Grigoropoulos, C. P.; Pan, H. Recrystallization of picosecond laser-melted ZnO nanoparticles in a liquid: A molecular dynamics study. *J. Chem. Phys.* **2010**, *132*, 164504.
(41) Shih, C.-Y.; Wu, C.; Shugaev, M. V.; Zhigilei, L. V. Atomistic modeling of nanoparticle generation in short pulse laser ablation of thin metal films in water. *J. Colloid Interface Sci.* **2017**, *489*, 3−17.
(42) Shih, C.-Y.; Shugaev, M. V.; Wu, C.; Zhigilei, L. V. Generation of subsurface voids, incubation effect, and formation of nanoparticles in short pulse laser interactions with bulk metal targets in liquid: molecular dynamics study. *J. Phys. Chem. C* **2017**, *121*, 16549−16567.
(43) Shih, C.-Y.; Streubel, R.; Heberle, J.; Letzel, A.; Shugaev, M. V.; Wu, C.; Schmidt, M.; Gökce, B.; Barcikowski, S.; Zhigilei, L. V. Two mechanisms of nanoparticle generation in picosecond laser ablation in liquids: the origin of the bimodal size distribution. *Nanoscale* **2018**, *10*, 6900−6910.
(44) Sun, J. M.; Gerstman, B. S.; Li, B. Bubble dynamics and shock waves generated by laser absorption of a photoacoustic sphere. *J. Appl. Phys.* **2000**, *88*, 2352−2362.
(45) Pustovalov, V. K.; Smetannikov, A. S.; Zharov, V. P. Photothermal and accompanied phenomena of selective nanophotothermolysis with gold nanoparticles and laser pulses. *Laser Phys. Lett.* **2008**, *5*, 775−792.
(46) Boulais, É.; Lachaine, R.; Meunier, M. Plasma mediated off-resonance plasmonic enhanced ultrafast laser-induced nanocavitation. *Nano Lett.* **2012**, *12*, 4763−4769.
(47) Lombard, J.; Biben, T.; Merabia, S. Kinetics of nanobubble generation around overheated nanoparticles. *Phys. Rev. Lett.* **2014**, *112*, 105701.
(48) Pyatenko, A.; Wang, H.; Koshizaki, N.; Tsuji, T. Mechanism of pulse laser interaction with colloidal nanoparticles. *Laser Photon. Rev.* **2013**, *7*, 596−604.
(49) Strasser, M.; Setoura, K.; Langbein, U.; Hashimoto, S. Computational modeling of pulsed laser-induced heating and evaporation of gold nanoparticles. *J. Phys. Chem. C* **2014**, *118*, 25748−25755.
(50) Delfour, L.; Itina, T. E. Mechanisms of ultrashort laser-induced fragmentation of metal nanoparticles in liquids: numerical insights. *J. Phys. Chem. C* **2015**, *119*, 13893−13900.
(51) Plech, A.; Kotaidis, V.; Lorenc, M.; Boneberg, J. Femtosecond laser near-field ablation from gold nanoparticles. *Nat. Phys.* **2006**, *2*, 44−47.
(52) Stavich, D.; Nestoiter, B.; Gonzalez, D.; Freund, A.; Buelna, X.; Wang, K.; Teprovich, J. A., Jr.; Eloranta, J. Time-resolved shadowgraph photography of laser-heated plasmonic gold nanoparticles in water. *J. Phys. Chem. C* **2020**, *124*, 14022−14029.
(53) Skripov, V. P. *Metastable Liquids*; Wiley, Israel Program for Scientific Translations: New York, Chichester, Jerusalem, London, 1974.
(54) Miotello, A.; Kelly, R. Laser-induced phase explosion: new physical problems when a condensed phase approaches the thermodynamic critical temperature. *Appl. Phys. A* **1999**, *69*, S67−S73.

https://doi.org/10.1021/acs.jpcc.1c03146
J. Phys. Chem. C 2021, 125, 13413−13432

(55) Garrison, B. J.; Itina, T. E.; Zhigilei, L. V. Limit of overheating and the threshold behavior in laser ablation. *Phys. Rev. E: Stat., Nonlinear, Soft Matter Phys.* **2003**, *68*, 041501.
(56) Shugaev, M. V.; He, M.; Levy, Y.; Mazzi, A.; Miotello, A.; Bulgakova, N. M.; Zhigilei, L. V. Laser-induced thermal processes: Heat transfer, generation of stresses, melting and solidification, vaporization and phase explosion. In *Handbook of Laser Micro- and Nano-Engineering*; Sugioka, K., Ed.; Springer: Cham, Switzerland, 2020; DOI: 10.1007/978-3-319-69537-2_11-1.
(57) Paltauf, G.; Dyer, P. E. Photomechanical processes and effects in ablation. *Chem. Rev.* **2003**, *103*, 487−518.
(58) Leveugle, E.; Ivanov, D. S.; Zhigilei, L. V. Photomechanical spallation of molecular and metal targets: molecular dynamics study. *Appl. Phys. A: Solids Surf.* **2004**, *79*, 1643−1655.
(59) Lin, Z.; Zhigilei, L. V. Thermal excitation of d band electrons in Au: implications for laser-induced phase transformations. *Proc. SPIE* **2006**, *6261*, 62610U.
(60) Zhigilei, L. V.; Garrison, B. J. Computer simulation study of damage and ablation of submicron particles from short-pulse laser irradiation. *Appl. Surf. Sci.* **1998**, *127−129*, 142−150.
(61) Zhigilei, L. V.; Garrison, B. J. Microscopic simulation of short pulse laser damage of melanin particles. *Proc. SPIE* **1998**, *3254*, 135−143.
(62) Fahdiran, R.; Urbassek, H. M. Ultrafast laser irradiation of spherical nanoparticles: molecular-dynamics results on fragmentation and small-angle scattering. *Eur. Phys. J. D* **2015**, *69*, 35.
(63) Werner, D.; Hashimoto, S. Improved working model for interpreting the excitation wavelength- and fluence-dependent response in pulsed laser-induced size reduction of aqueous gold nanoparticles. *J. Phys. Chem. C* **2011**, *115*, 5063−5072.
(64) Yamada, K.; Tokumoto, Y.; Nagata, T.; Mafuné, F. Mechanism of laser-induced size-reduction of gold nanoparticles as studied by nanosecond transient absorption spectroscopy. *J. Phys. Chem. B* **2006**, *110*, 11751−11756.
(65) Meesungnoen, J.; Jay-Gerin, J.-P.; Filali-Mouhim, A.; Mankhetkorn, S. Low-energy electron penetration range in liquid water. *Radiat. Res.* **2002**, *158*, 657−660.
(66) Riffe, D. M.; More, R. M.; Wang, X. Y.; Downer, M. C.; Fisher, D. L.; Tajima, T.; Erskine, J. L. Femtosecond thermionic emission from metals in the space-charge-limited regime. *J. Opt. Soc. Am. B* **1993**, *10*, 1424−1435.
(67) Wendelen, W.; Autrique, D.; Bogaerts, A. Space charge limited electron emission from a Cu surface under ultrashort pulsed laser irradiation. *Appl. Phys. Lett.* **2010**, *96*, 051121.
(68) Bulgakova, N. M.; Rosenfeld, A.; Ehrentraut, L.; Stoian, R.; Hertel, I. V. Modeling of electron dynamics in laser-irradiated solids: Progress achieved through a continuum approach and future prospects. *Proc. SPIE* **2007**, *6732*, 673208.
(69) Ivanov, D. S.; Zhigilei, L. V. Combined atomistic-continuum modeling of short-pulse laser melting and disintegration of metal films. *Phys. Rev. B: Condens. Matter Mater. Phys.* **2003**, *68*, 064114.
(70) Wu, C.; Zhigilei, L. V. Microscopic mechanisms of laser spallation and ablation of metal targets from large-scale molecular dynamics simulations. *Appl. Phys. A* **2014**, *114*, 11−32.
(71) Tabetah, M.; Matei, A.; Constantinescu, C.; Mortensen, N. P.; Dinescu, M.; Schou, J.; Zhigilei, L. V. The minimum amount of "matrix" needed for matrix-assisted pulsed laser deposition of biomolecules. *J. Phys. Chem. B* **2014**, *118*, 13290−13299.
(72) Zou, J.; Wu, C.; Robertson, W. D.; Zhigilei, L. V.; Miller, R. J. D. Molecular dynamics investigation of desorption and ion separation following picosecond infrared laser (PIRL) ablation of an ionic aqueous protein solution. *J. Chem. Phys.* **2016**, *145*, 204202.
(73) Zhigilei, L. V.; Garrison, B. J. Pressure waves in microscopic simulations of laser ablation. *Mater. Res. Soc. Symp. Proc.* **1999**, *538*, 491−496.
(74) Schäfer, C.; Urbassek, H. M.; Zhigilei, L. V.; Garrison, B. J. Pressure-transmitting boundary conditions for molecular-dynamics simulations. *Comput. Mater. Sci.* **2002**, *24*, 421−429.
(75) Karim, E. T.; Shugaev, M.; Wu, C.; Lin, Z.; Hainsey, R. F.; Zhigilei, L. V. Atomistic simulation study of short pulse laser interactions with a metal target under conditions of spatial confinement by a transparent overlayer. *J. Appl. Phys.* **2014**, *115*, 183501.
(76) Frenkel, D.; Smit, B. *Understanding Molecular Simulation: From Algorithms to Applications*; Academic Press: San Diego, 1996.
(77) Zhigilei, L. V.; Lin, Z.; Ivanov, D. S.; Leveugle, E.; Duff, W. H.; Thomas, D.; Sevilla, C.; Guy, S. J. Atomic/molecular-level simulations of laser-materials interactions. In *Laser-Surface Interactions for New Materials Production: Tailoring Structure and Properties*; Springer Series in Materials Science; Miotello, A., Ossi, P., Eds.; Springer Verlag: New York, 2010; Vol. *130*, pp 43−79; DOI: 10.1007/978-3-642-03307-0_3.
(78) Anisimov, S. I.; Kapeliovich, B. L.; Perel'man, T. L. Electron emission from metal surfaces exposed to ultrashort laser pulses. *Sov. Phys.—JETP* **1974**, *39*, 375−377.
(79) Note that the use of the term "lattice temperature" does not imply the preservation of the crystalline order in the irradiated material but is simply follows terminology established in the literature presenting TTM calculations. The lattice temperature here refers to the temperature associated with thermal atomic motion, regardless of the phase state of the material.
(80) Ivanov, D. S.; Zhigilei, L. V. Combined atomistic-continuum model for simulation of laser interaction with metals: Application in the calculation of melting thresholds in Ni targets of varying thickness. *Appl. Phys. A: Mater. Sci. Process.* **2004**, *79*, 977−981.
(81) The equivalent diameter D_e of a nanoparticle is the diameter of a spherical particle with the same number of atoms N defined as $D_e = \sqrt[3]{3N/2\pi}\,a$, where a is the lattice parameters of a Au fcc crystal at 300 K.
(82) The distinction between Au nanoparticles ($D_e \geq 2.2$) and atomic clusters ($D_e < 2.2$ nm) is made based on the electronic structure, as reflected by the presence or absence of surface plasmon resonance in the absorption spectrum.
(83) Hohlfeld, J.; Wellershoff, S.-S.; Güdde, J.; Conrad, U.; Jähnke, V.; Matthias, E. Electron and lattice dynamics following optical excitation of metals. *Chem. Phys.* **2000**, *251*, 237−258.
(84) Lin, Z.; Zhigilei, L. V.; Celli, V. Electron-phonon coupling and electron heat capacity of metals under conditions of strong electron-phonon nonequilibrium. *Phys. Rev. B: Condens. Matter Mater. Phys.* **2008**, *77*, 075133.
(85) Stella, A.; Nisoli, M.; De Silvestri, S.; Svelto, O.; Lanzani, G.; Cheyssac, P.; Kofman, R. Size effects in the ultrafast electronic dynamics of metallic tin nanoparticles. *Phys. Rev. B: Condens. Matter Mater. Phys.* **1996**, *53*, 15497−15500.
(86) Nisoli, M.; Stagira, S.; De Silvestri, S.; Stella, A.; Tognini, P.; Cheyssac, P.; Kofman, R. Ultrafast electronic dynamics in solid and liquid gallium nanoparticles. *Phys. Rev. Lett.* **1997**, *78*, 3575−3578.
(87) Del Fatti, N.; Flytzanis, C.; Vallée, F. Ultrafast induced electron-surface scattering in a confined metallic system. *Appl. Phys. B* **1999**, *68*, 433−437.
(88) Arbouet, A.; Voisin, C.; Christofilos, D.; Langot, P.; Fatti, N. D.; Vallée, F.; Lermé, J.; Celep, G.; Cottancin, E.; Gaudry, M.; Pellarin, M.; Broyer, M.; Maillard, M.; Pileni, M. P.; Treguer, M. Electron-phonon scattering in metal clusters. *Phys. Rev. Lett.* **2003**, *90*, 177401.
(89) Darugar, Q.; Qian, W.; El-Sayed, M. A.; Pileni, M.-P. Size-dependent ultrafast electronic energy relaxation and enhanced fluorescence of copper nanoparticles. *J. Phys. Chem. B* **2006**, *110*, 143−149.
(90) Hartland, G. V. Optical studies of dynamics in noble metal nanostructures. *Chem. Rev.* **2011**, *111*, 3858−3887.
(91) Mongin, D.; Maioli, P.; Burgin, J.; Langot, P.; Cottancin, E.; D'Addato, S.; Canut, B.; Treguer, M.; Crut, A.; Vallée, F.; Del Fatti, N. Ultrafast electron-lattice thermalization in copper and other noble metal nanoparticles. *J. Phys.: Condens. Matter* **2019**, *31*, 084001.
(92) Smith, B. A.; Zhang, J. Z.; Giebel, U.; Schmid, G. Direct probe of size-dependent electronic relaxation in single-sized Au and nearly

monodisperse Pt colloidal nano-particles. *Chem. Phys. Lett.* **1997**, *270*, 139−144.
(93) Yau, S. H.; Varnavski, O.; Gilbertson, J. D.; Chandler, B.; Ramakrishna, G.; Goodson, T., III Ultrafast optical study of small gold monolayer protected clusters: A closer look at emission. *J. Phys. Chem. C* **2010**, *114*, 15979−15985.
(94) Link, S.; El-Sayed, M. A.; Schaaff, T. G.; Whetten, R. L. Transition from nanoparticle to molecular behavior: a femtosecond transient absorption study of a size-selected 28 atom gold cluster. *Chem. Phys. Lett.* **2002**, *356*, 240−246.
(95) Varnavski, O.; Ramakrishna, G.; Kim, J.; Lee, D.; Goodson, T. Critical size for the observation of quantum confinement in optically excited gold clusters. *J. Am. Chem. Soc.* **2010**, *132*, 16−17.
(96) Mustalahti, S.; Myllyperkiö, P.; Malola, S.; Lahtinen, T.; Salorinne, K.; Koivisto, J.; Häkkinen, H.; Pettersson, M. Molecule-like photodynamics of $Au_{102}(pMBA)_{44}$ nanocluster. *ACS Nano* **2015**, *9*, 2328−2335.
(97) Zhou, M.; Zeng, C.; Chen, Y.; Zhao, S.; Sfeir, M. Y.; Zhu, M.; Jin, R. Evolution from the plasmon to exciton state in ligand-protected atomically precise gold nanoparticles. *Nat. Commun.* **2016**, *7*, 13240.
(98) Koop, A.; Gantefoer, G.; Kim, Y. D. Long-lived excited states in metal clusters. *Phys. Chem. Chem. Phys.* **2017**, *19*, 21335−21339.
(99) Bilotsky, Y.; Tomchuk, P. M. Size effect in electron-lattice energy exchange in small metal particles. *Surf. Sci.* **2006**, *600*, 4702−4711.
(100) Link, S.; Burda, C.; Wang, Z. L.; El-Sayed, M. A. Electron dynamics in gold and gold-silver alloy nanoparticles: The influence of a nonequilibrium electron distribution and the size dependence of the electron-phonon relaxation. *J. Chem. Phys.* **1999**, *111*, 1255−1264.
(101) Dowgiallo, A.-M.; Knappenberger, K. L., Jr. Ultrafast electron-phonon coupling in hollow gold nanospheres. *Phys. Chem. Chem. Phys.* **2011**, *13*, 21585−21592.
(102) Hartland, G. V. Electron-phonon coupling and heat dissipation in metal nanoparticles. *Int. J. Nanotechnol.* **2004**, *1*, 307−327.
(103) Aruda, K. O.; Tagliazucchi, M.; Sweeney, C. M.; Hannah, D. C.; Schatz, G. C.; Weiss, E. A. Identification of parameters through which surface chemistry determines the lifetimes of hot electrons in small Au nanoparticles. *Proc. Natl. Acad. Sci. U.S.A.* **2013**, *110*, 4212−4217.
(104) Lisinetskaya, P. G.; Braun, C.; Proch, S.; Kim, Y. D.; Ganteför, G.; Mitrić, R. Excited state nonadiabatic dynamics of bare and hydrated anionic gold clusters $Au_3^-[H_2O]_n$ (n = 0-2). *Phys. Chem. Chem. Phys.* **2016**, *18*, 6411−6419.
(105) Lin, Z.; Zhigilei, L. V. Thermal excitation of d band electrons in Au: Implications for laser-induced phase transformations. *Proc. SPIE* **2006**, *6261*, 62610U.
(106) Wood, D. M.; Ashcroft, N. W. Quantum size effects in the optical properties of small metallic particles. *Phys. Rev. B: Condens. Matter Mater. Phys.* **1982**, *25*, 6255−6274.
(107) Simoni, J.; Daligault, J. First-principles determination of electron-ion couplings in the warm dense matter regime. *Phys. Rev. Lett.* **2019**, *122*, 205001.
(108) Hostetler, J. L.; Smith, A. N.; Czajkowsky, D. M.; Norris, P. M. Measurement of the electron-phonon coupling factor dependence on film thickness and grain size in Au, Cr, and Al. *Appl. Opt.* **1999**, *38*, 3614−3620.
(109) Huang, W.; Qian, W.; El-Sayed, M. A.; Ding, Y.; Wang, Z. L. Effect of the lattice crystallinity on the electron−phonon relaxation rates in gold nanoparticles. *J. Phys. Chem. C* **2007**, *111*, 10751−10757.
(110) Mattson, W.; Rice, B. M. Near-neighbor calculations using a modified cell-linked list method. *Comput. Phys. Commun.* **1999**, *119*, 135−148.
(111) Kittel, C. *Introduction to Solid State Physics*, 8th ed.; John Wiley & Sons, Inc: Hoboken, NJ, 2005.
(112) Howe, J. M. *Interfaces in Materials: Atomic Structure, Thermodynamics and Kinetics of Solid-Vapor, Solid-Liquid and Solid-Solid Interfaces*; Wiley: New York, 1997.
(113) Laven, P. http://www.philiplaven.com/mieplot.htm (accessed on December 10, 2020).
(114) Pyatenko, A.; Yamaguchi, M.; Suzuki, M. Mechanisms of size reduction of colloidal silver and gold nanoparticles irradiated by Nd:YAG laser. *J. Phys. Chem. C* **2009**, *113*, 9078−9085.
(115) The temperature rise per unit of fluence, evaluated from Mie theory calculations for a 54 nm nanoparticle irradiated at 532 nm in water is 41 $K/(Jm^{-2})$, which is more than 4 times higher than the slope of the temperature versus fluence dependence of 8.5 $K/(Jm^{-2})$ determined experimentally in ref 25. The theoretical value of 31 $K/(Jm^{-2})$ provided in ref 25 is an underestimation, as confirmed through communication with the authors.
(116) Link, S.; El-Sayed, M. A. Shape and size dependence of radiative, non-radiative and photothermal properties of gold nanocrystals. *Int. Rev. Phys. Chem.* **2000**, *19*, 409−453.
(117) Zhakhovskii, V. V.; Inogamov, N. A.; Petrov, Y. V.; Ashitkov, S. I.; Nishihara, K. Molecular dynamics simulation of femtosecond ablation and spallation with different interatomic potentials. *Appl. Surf. Sci.* **2009**, *255*, 9592−9596.
(118) Hu, H.; Sun, Y. Effect of nanopatterns on Kapitza resistance at a water-gold interface during boiling: A molecular dynamics study. *J. Appl. Phys.* **2012**, *112*, 053508.
(119) Zhigilei, L. V.; Ivanov, D. S. Channels of energy redistribution in short-pulse laser interactions with metal targets. *Appl. Surf. Sci.* **2005**, *248*, 433−439.
(120) Landau, L. D.; Lifshitz, E. M. *Mechanics*, 3rd ed.; Pergamon Press: Oxford, New York, 1976.
(121) Matsumoto, M.; Tanaka, K. Nano bubble-Size dependence of surface tension and inside pressure. *Fluid Dyn. Res.* **2008**, *40*, 546−553.
(122) Turner, M.; Golovko, V. B.; Vaughan, O. P. H.; Abdulkin, P.; Berenguer-Murcia, A.; Tikhov, M. S.; Johnson, B. F. G.; Lambert, R. M. Selective oxidation with dioxygen by gold nanoparticle catalysts derived from 55-atom clusters. *Nature* **2008**, *454*, 981−983.
(123) Templeton, A. C.; Wuelfing, W. P.; Murray, R. W. Monolayer-protected cluster molecules. *Acc. Chem. Res.* **2000**, *33*, 27−36.
(124) Sylvestre, J.-P.; Poulin, S.; Kabashin, A. V.; Sacher, E.; Meunier, M.; Luong, J. H. T. Surface chemistry of gold nanoparticles produced by laser ablation in aqueous media. *J. Phys. Chem. B* **2004**, *108*, 16864−16869.
(125) Letzel, A.; Gökce, B.; Wagener, P.; Ibrahimkutty, S.; Menzel, A.; Plech, A.; Barcikowski, S. Size quenching during laser synthesis of colloids happens already in the vapor phase of the cavitation bubble. *J. Phys. Chem. C* **2017**, *121*, 5356−5365.
(126) Letzel, A.; Reich, S.; dos Santos Rolo, T.; Kanitz, A.; Hoppius, J.; Rack, A.; Olbinado, M. P.; Ostendorf, A.; Gökce, B.; Plech, A.; Barcikowski, S. Time and mechanism of nanoparticle functionalization by macromolecular ligands during pulsed laser ablation in liquids. *Langmuir* **2019**, *35*, 3038−3047.
(127) Ziefuß, A. R.; Barcikowski, S.; Rehbock, C. Synergism between specific halide anions and pH effects during nanosecond laser fragmentation of ligand-free gold nanoparticles. *Langmuir* **2019**, *35*, 6630−6639.
(128) Combe, N.; Jensen, P.; Pimpinelli, A. Changing shapes in the nanoworld. *Phys. Rev. Lett.* **2000**, *85*, 110.
(129) Compagnini, G.; Scalisi, A. A.; Puglisi, O. Production of gold nanoparticles by laser ablation in liquid alkanes. *J. Appl. Phys.* **2003**, *94*, 7874−7877.
(130) Poletti, A.; Fracasso, G.; Conti, G.; Pilot, R.; Amendola, V. Laser generated gold nanocorals with broadband plasmon absorption for photothermal applications. *Nanoscale* **2015**, *7*, 13702.
(131) Harris, N.; Ford, M. J.; Mulvaney, P.; Cortie, M. B. Tunable infrared absorption by metal nanoparticles: the case for gold rods and shells. *Gold Bull.* **2008**, *41*, 5−14.
(132) Mackey, M. A.; Ali, M. R. K.; Austin, L. A.; Near, R. D.; El-Sayed, M. A. The most effective gold nanorod size for plasmonic photothermal therapy: Theory and in vitro experiments. *J. Phys. Chem. B* **2014**, *118*, 1319−1326.